# Numerical Study of Flow Structure and Aerodynamic Noise Characteristics of Rectangular Jets with Different Nozzle Shapes at Low Mach Number

Yuan He[a)] and David Angland

*Faculty of Engineering and Physical Sciences, University of Southampton, Southampton, SO16 7QF, United Kingdom*

(Dated: 9 December 2025)

This study numerically investigates the flow and aeroacoustic characteristics of rectangular jets with different nozzle geometries but with the same mass flow rate. Turbulence statistics in the near field are compared, and the influence of nozzle shape on jet dynamics and associated noise is assessed. The configurations analysed include a planar nozzle and orifice-type nozzles with square, bevelled and filleted edges. The Reynolds number based on the nozzle height is $1.1 \times 10^4$ and the maximum Mach number is approximately 0.17. Flow fields are computed using Delayed Detached Eddy Simulation with the Spalart-Allmaras turbulence model, while far-field noise is obtained using Farrasat's 1A formulation from permeable integration surfaces. The numerical framework is validated against experimental data. Results demonstrate that square and bevelled orifices induce vena contraction effect by their sharp edges, resulting in higher exit velocities and elevated near-field turbulence. In contrast, planar and filleted nozzles exhibit weaker turbulence, delayed shear layer roll-up, and longer potential cores. The bevelled orifice in particular exhibits pronounced tonal noise peaks at 4.3 kHz, 8.5 kHz, and 12.7 kHz in the turbulent velocity spectrum. Spectral proper orthogonal decomposition identified dominant energetic modes near the potential core boundary where vortex roll-up and shear-layer interaction occur. The sharp-edged orifices produce overall sound pressure levels approximately 10 dB higher when integrating across the full frequency spectrum (including the tones) and 7 dB higher for the broadband component, compared to the planar and filleted nozzles. These findings underscore the trade-off between jet mixing and noise mitigation in nozzle design, offering insights for optimizing rectangular jets for engineering.

---

[a)] yh6y23@soton.ac.uk

# I. INTRODUCTION

Rectangular jets exhibit unique and distinct flow characteristics compared to circular jets. They have applications in aerodynamic flow control, noise control and blowing applications. Examples include noise reduction in aircraft[1,2] and high-speed trains[3], high-velocity hand dryers in public restrooms[4], and enhanced mixing of air and fuel in combustion systems[5,6]. For instance, a practical application of rectangular jets is in the flow control of bluff body wakes. Although many studies have been conducted to reduce the noise generated by cylinders[7,8], the potential of rectangular jets in this context remains significant[9,10]. The growing interest in rectangular jets has led to increased focus on aspects such as aerodynamic efficiency and noise reduction. This necessitates a comprehensive understanding of rectangular jet dynamics and the potential influential factors, such as nozzle profiles, aspect ratio, Reynolds number and inlet boundary conditions. Such a fundamental understanding is critical for expanding their applications across diverse sectors.

A circular jet spreads uniformly in all directions, whereas rectangular jets exhibit distinct spreading rates along their major and minor axes, leading to a flow that is no longer axisymmetric, particularly in the near-field region of the jet nozzle. As shown in Fig. 1, the major axes refer to the jet width direction (Z direction), while the minor axes refer to the jet height direction (Y direction). For a rectangular jet nozzle, the aspect ratio is defined as the ratio between the jet width and jet height. When the aspect ratio becomes sufficiently large, the flow field exhibits approximately two-dimensional characteristics. In this case, the rectangular jet is referred to as a ‘planar jet’ as the flow properties are predominantly confined to a plane that is orthogonal to the major axes.

Sfeir[11,12] experimentally studied the three-dimensional flow properties of a rectangular jet with different aspect ratios (10 to 60) using hot-wire anemometry. They found that, for a Reynolds number of $1.22 \times 10^4$, based on jet height, there are limited changes in the centreline velocity decay, spreading rate and turbulence intensity with changes in aspect ratio. However, for a lower Reynolds number of $0.37 \times 10^4$, the effect of aspect ratio becomes more significant. At lower values of aspect ratio, at this Reynolds number, the centreline velocity decay, spreading rate and turbulence intensity behaviour is different to two-dimensional jet behaviour. As the aspect ratio increases, these differences become smaller. In an experiment, with aspect ratios ranging from 2 to 20, Quinn[13] demonstrated that higher aspect ratios increase mixing rates, reduce the length of the potential core, and increase turbulence kinetic energy in the shear layers. Deo et al.[14]

systematically studied the effect of aspect ratio on the flow properties of rectangular jets experimentally. Their research aligned with Quinn[15] and also showed that increasing the nozzle aspect ratio enhances jet spreading and mixing efficiency.

Deo et al.[16] expanded upon this work by investigating the influence of Reynolds number on rectangular jets. Their findings indicate that a rectangular jet is sensitive to the nozzle exit conditions, such as velocity profile, turbulence intensity and nozzle geometry, at Reynolds numbers below $10^4$, based on jet height. However, this sensitivity decreases as the Reynolds number increases. This observation is consistent with the findings from Sfeir[12]. Similar to circular jet flow, a Reynolds number of $10^4$ is a critical threshold in rectangular jet flows. It often marks a transitional regime where the flow evolves from a laminar-like regime with coherent shear layers to a fully turbulent state characterized by enhanced mixing, breakdown of organized vortices, and increased jet spreading rates due to intensified turbulent entrainment and three-dimensional vortex interactions[16,17]. This makes it an important condition for understanding jet dynamics and designing systems involving jet flows.

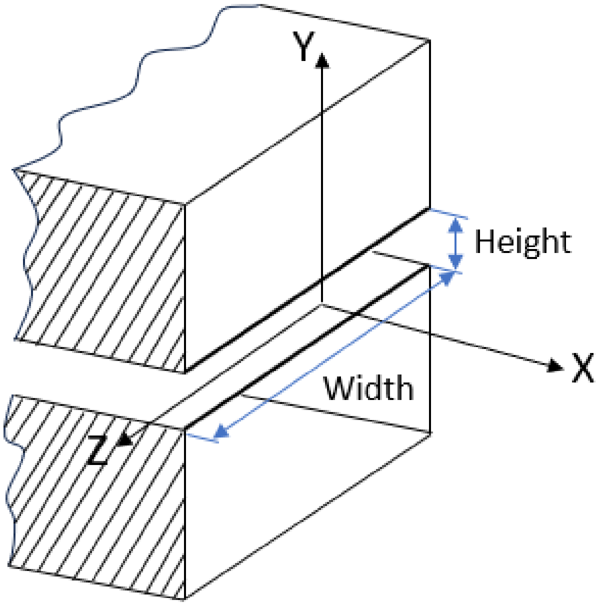

FIG. 1: Schematic of a planar jet.

The aspect ratio, Reynolds number and inlet conditions have all been identified as factors influencing the behaviour of rectangular jet flows. Another crucial factor is the nozzle geometry. In the study by Sfeir[11], two types of nozzles were tested. One consisted of rectangular slots with sharp edges, while the other one featured rectangular channels with a length equal to fifty times the slot height. In the experiment, the nozzle geometry was found to significantly influence both the velocity and temperature fields, such as velocity and temperature decay along the centreline, the velocity profile along the major axis (Z direction in Fig. 1), and the jet width distribution. In a follow-up experiment, Sfeir[12] found that jets emanating from long rectangular channels have shorter development lengths than those from sharp-edged orifices. The flow also remains more uniform in the X–Z plane (as defined in Fig. 1) over extended downstream distances. In contrast, jets from sharp orifices, particularly those with small aspect ratios, are less likely to develop into self-preserving two-dimensional flows. The characteristic ’saddle-back’ velocity profile along the major axis is more pronounced in these cases than in jets from long rectangular channels.

Further insights from Deo et al.[18] revealed that the geometric profile of nozzle exits, such as sharp or filleted edges, directly impacts the shear layer interactions, turbulence intensity, and downstream flow stability, emphasizing how shape-specific features of the nozzle govern jet behaviour. Abdel-Rahman[19] reviewed the relevant research and highlighted that nozzle shape dictates the initial shear layer formation and turbulence at the jet exit, leading to variations in mixing and spreading rates. Together, these findings demonstrate that nozzle shape significantly alters the flow field by changing turbulent structures and mixing efficiency, making it a critical design parameter in engineering applications.

As well as the experimental research, numerical studies have also been conducted to investigate the flow properties of rectangular jets. To simplify the analysis, computational models were often reduced to limited span representations with periodic boundary conditions applied in the simulations. Early work by Le Ribault et al.[20,21] employed large eddy simulations (LES) to study planar jets, revealing insights into the development of the shear layers and demonstrating the accuracy of LES in capturing jet flow dynamics. A recent study by Matsuyama[22] also employed LES but with an implicit sub-grid viscosity model to study the near-field turbulence properties of a rectangular jet at a Reynolds number of $10^4$. This study shows the accuracy of implicit LES in resolving these multi-scale interactions without requiring subgrid-scale modelling, providing robust predictions of jet spreading rates and turbulence intensities.

In addition to LES, direct numerical simulation offers resolution of turbulence without relying on sub-grid scale models, as demonstrated in studies of transitional rectangular jets[22,23]. These investigations provided benchmark data for validating turbulence models and highlighted the importance of the initial conditions in determining jet evolution. Due to the computational cost of LES and Direct Numerical Simulation (DNS), the jet nozzle geometry is often replaced by a simplified inlet boundary condition, and the flow is simulated under the assumption of infinite spanwise extent using periodic boundary conditions. Few studies have considered the three-dimensional effect from the jet nozzle aspect ratio and moved beyond the infinite spanwise assumption[24,25]. These investigations demonstrate that near-field turbulence statistics are significantly influenced by nozzle geometry and boundary conditions, whereas in the far-field the flow transitions towards self-similarity. The study of Jiang et al.[25] also shows the frequency characteristics of coherent structures in rectangular jets and identifies dominant frequencies that govern vortex roll-up in the shear layer, entrainment and transition from organized instabilities to fully developed turbulent flow downstream. These findings provide insights into jet flow behaviours and its associated phenomena.

While previous experimental and numerical studies have explored the influence of nozzle geometry on the development of rectangular jets, their focus has primarily been on statistical flow properties. Although some recent studies have used high-fidelity numerical methods to investigate the noise generation mechanisms of jet flows, they primarily focus on circular jets[26–28]. While several experimental studies have examined the effects of nozzle geometry on jet flows[11,12,18], most of these investigations focused on the aerodynamic characteristics, with limited attention given to the aerodynamic noise and detailed flow dynamics. The aeroacoustic noise generated by rectangular jets has attracted increased attention also motivating this current work. Furthermore, the near-field flow features of rectangular nozzles, e.g. vena contraction, vortex development and entrainment, have not been systematically reported for different nozzle geometries. In this work, the different nozzle geometries have the same mass flow rate allowing them to be directly compared and effect of the nozzle shape isolated. In addition, existing numerical simulations often simplify the nozzle inlet conditions by prescribing predefined velocity profiles instead of modelling the actual nozzle geometry. This simplification limits the ability to accurately capture the influence of nozzle shape on the jet behaviour and its resultant acoustic characteristics.

To address this gap, this study conducts numerical simulations aimed at investigating the impact of nozzle geometries on the near-field turbulence statistics, jet dynamics and the aerodynamic noise of rectangular jets, which are commonly used in engineering applications. The novelty of this work lies in the first-time investigation of both jet dynamics and aerodynamic noise in different rectangular jet configurations. The nozzle configurations analyzed include a planar nozzle and orifice-type nozzles with square, bevelled, and filleted edges. These geometries have wide engineering applications and have been studied by researchers[11–13,15,18,29]. By comparing the flow field, jet dynamics, and aeroacoustic characteristics of the four configurations, the influence of nozzle geometry will be quantitatively assessed. The near-field turbulence statistics, vortex roll-up frequencies, and noise levels will be evaluated. The findings will facilitate the selection and design of rectangular nozzles, supporting trade-offs between jet mixing and acoustic noise in engineering applications.

To balance the simulation accuracy and computational cost, fully compressible Delayed Detached Eddy Simulation with the Spalart-Allmaras turbulence model is employed to simulate the flow field. This approach enables the numerical investigation of various nozzle geometries while maintaining both accuracy and affordable computational cost. To calculate the far-field noise, the free-space time-domain solution of the Ffowcs Williams-Hawkings equations (Farassat 1A formulation) will be used. To isolate the effect of nozzle shape and to exclude other influential factors, the simulations will be performed under the infinite spanwise length assumption similar to the boundary conditions used in the numerical studies discussed previously. The bulk flow velocity of all the simulation will be kept constant and the Reynolds number based on the bulk flow velocity and the height of the jet is approximately $1.1 \times 10^4$. Spectral Proper Orthogonal Decomposition (SPOD) is employed to analyze the flow field, offering detailed insights into the spatial distribution and influence of dominant flow modes and their correlation with the radiated acoustic noise. The paper begins with an overview of the numerical methods, followed by details of the computational domain, grid discretization, and numerical validations. Finally, it presents an analysis of the results for various rectangular jet geometries and their effects on near-field turbulence, flow dynamics and aerodynamic noise.

## II. NUMERICAL BACKGROUND

### A. Delayed Detached Eddy Simulation

In this work, the compressible Navier–Stokes (N-S) equations are adopted, even though the highest Mach number at the nozzle exit in some cases is only approximately 0.17. Detached Eddy Simulation (DES), which combines Large Eddy Simulation (LES) and Unsteady Reynolds-Averaged Navier-Stokes (URANS), is chosen to balance simulation accuracy and computational cost. DES was firstly proposed by Spalart et al.[30]. In this method, regions near solid boundaries are simulated using URANS, while LES is applied outside these regions. As a result, the computational cost of DES is considerably reduced compared to LES. DES is not a zonal approach because the switch between URANS and LES is determined by the local grid near the solid wall, rather than a predetermined parameter setting for specific zones. The switch is applied by replacing the length scale by the minimum of the wall distance and a grid-based length. However, in separation or transition flows, which are sensitive to the grid and turbulence models, grid-induced separation may occur at the edge of the boundary layer depending on the computational mesh[31,32]. Therefore, Spalart et al.[33] proposed a new treatment to over this issue, which is known as Delayed Detached-Eddy Simulation (DDES). Compared with the DES method, the length scale in DDES is not only dependent on the grid but also on the flow field variables. This improves predictions, particularly for cases involving flow separation, and has been validated in simulations across various scales[34–36]. The detailed equations can be found in Spalart et al.[33]. To ensure consistency with prior studies and to ensure a reasonable computational cost, the DDES methodology is adopted in the present work.

### B. Ffowcs Williams & Hawkings Equation

The Ffowcs Williams–Hawkings (FW-H) method is an acoustic analogy that extends Lighthill's equation to predict sound generated by moving bodies and turbulent flows by integrating flow quantities over a control surface surrounding the noise sources. Farassat's Formulation 1A is a solution to the Ffowcs Williams and Hawkings (FW-H) equation in free space, where the solid surfaces move at subsonic speeds. The detailed derivation of this formula can be found in Farassat[37]. It is expressed as:

$$\begin{aligned} 4\pi p'_T(\mathbf{x},t) = &\int_{f=0} \frac{\rho_0\left(\dot{U}_n + U_{\dot{n}}\right)}{r\left(1-M_r\right)^2}\,\mathrm{d}S \\ &+ \int_{f=0} \frac{\rho_0 U_n\left\{r\dot{M}_r + c_0(M_r - M^2)\right\}}{r^2\left(1-M_r\right)^3}\,\mathrm{d}S, \end{aligned} \tag{1}$$

$$\begin{aligned} 4\pi p'_L(\mathbf{x},t) = &\frac{1}{c_0}\int_{f=0} \frac{\dot{L}_r}{r(1-M_r)^2}\,\mathrm{d}S + \int_{f=0} \frac{L_r - L_M}{r^2(1-M_r)^2}\,\mathrm{d}S \\ &+ \frac{1}{c_0}\int_{f=0} \frac{L_r\left\{r\dot{M}_r + c_0(M_r - M^2)\right\}}{r^2(1-M_r)^3}\,\mathrm{d}S, \end{aligned} \tag{2}$$

where $c_0$ amd $\rho_0$ denote the sound speed and air density in the farfield, $r$ is distance to the observer, $S$ is the integral surface and $M$ is the Mach number. Eq.(1) is the thickness noise ($p'_T$) and Eq.(2) is the loading noise ($p'_L$). The dot above a variable ($\cdot$) denotes the time derivative. The condition $f =$

0 indicates that the variables are evaluated on the integration surface. The subscripted quantities are the dot products between a vector and the unit vector implied by the subscript. For example, $M_r = M \cdot \mathbf{r}$, where **n** and **r** represent the surface normal unit vector ($\hat{n}_i$) and the radiation direction unit vector ($\hat{r}_i$) respectively. $U_i = v_i + \rho/\rho_0(u_i - v_i)$, where $u_i$ denotes the fluid velocity and $v_i$ denotes the surface velocity. The loading source term is defined as $L_i = P_{ij}\hat{n}_j + \rho u_i(u_n - v_n)$, where $P_{ij}$ is the compressible stress tensor. An in-house FW-H solver based on permeable FW-H integral surfaces was used in this study.

## III. SETUP AND VALIDATION

### A. Geometry and numerical settings

Four nozzle configurations are considered in this study, as illustrated in Fig. 2. These are a planar nozzle, a square-edge orifice, a bevelled-edge orifice, and a filleted-edge orifice. The planar nozzle, as shown in Fig. 2(a), allows the inlet flow to develop before exit and serves as the baseline case due to its simplicity and practical relevance. The orifice-type nozzles (Fig. 2(b) to (d)) feature a finite wall thickness of 2 mm and a nozzle height of 4 mm. The bevelled orifice has a 45° edge angle, while the filleted orifice includes a 2 mm internal radius. These nozzle configurations are relevant and similar configurations have been investigated experimentally in rectangular jets in different studies by Sfeir[12], Quinn[13] and Deo et al.[18]. This present work examines the near-field turbulence, jet dynamics, and aerodynamic noise associated with these nozzle geometries systematically at the same mass flow rate.

Fig. 3 shows the computational domain for the jet flow using the planar nozzle as an example. The domain was designed to ensure full jet development without boundary effects while maintaining computational efficiency. The downstream outlet is located $300h$ from the front outlet and $5h$ from the front wall, with a $200h$ spacing between the top and bottom boundaries. The front wall (planar case) and the orifice chamber both have a width of $10h$, providing a balance between accuracy and cost. Free-outflow and non-reflective pressure boundary conditions were applied at the outlet, front outlet, and upper and lower planes to prevent wave reflection[38], while no-slip conditions were enforced on all solid walls. Periodic boundaries in the spanwise direction simulate an infinite span, following common practice for reducing computational expense[22]. The rationale for the chosen spanwise length is discussed in the next section.

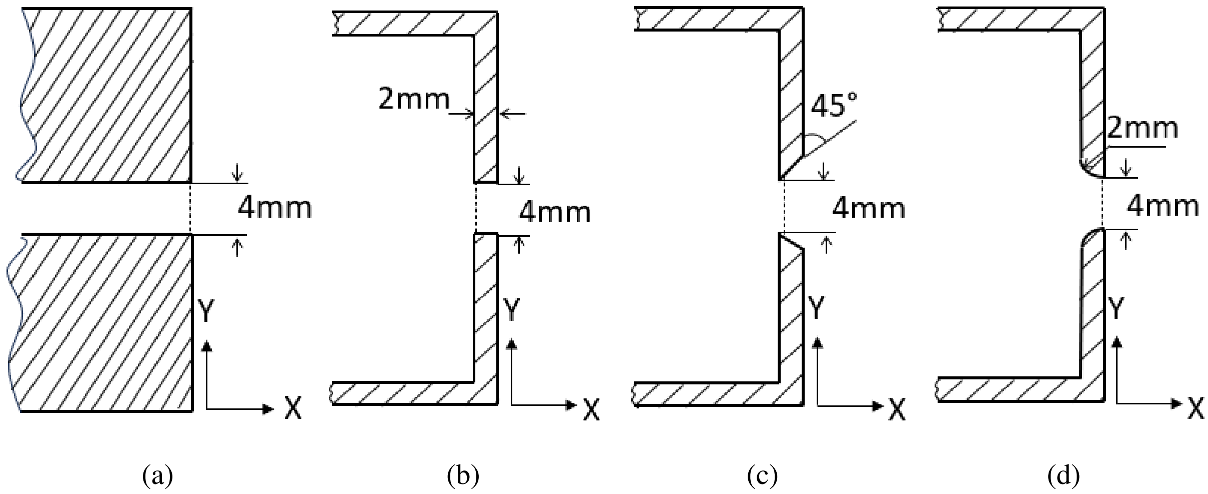

(a) (b) (c) (d)

FIG. 2: Different shapes of jet exits, (a) planar nozzle; (b) square-edge orifice; (c) bevelled-edge orifice; (d) filleted-edge orifice. The dashed lines denote the minimum cross-sectional area of the nozzle.

As demonstrated in the studies of Deo et al.[16], the flow characteristics of a rectangular jet exhibit a pronounced dependence on the Reynolds number ($\mathrm{Re} = U_b h/\nu$) below $10^4$. However, this dependency becomes less significant as the Reynolds number exceeds $10^4$, marking a transition towards behaviour more characteristic of fully turbulent jets. This transition is of critical importance in the study of rectangular jet flows. Therefore, in the present study, a Re of $1.1 \times 10^4$ is selected, achieved by setting the jet height ($h$) to 4 mm and the mean bulk flow velocity ($U_b$) to 40 m/s. $U_b$ is defined as,

$$U_b = \frac{\int_A \rho \left(\mathbf{U} \cdot \mathbf{n}\right) \mathrm{d}A}{\int_A \rho \, \mathrm{d}A}, \tag{3}$$

where $\rho$ is the density, $\mathbf{U}$ is the time-averaged velocity vector, $\mathbf{n}$ is cross section unit normal vector, and $A$ is the cross sectional area. $\int_A \rho \left(\mathbf{U} \cdot \mathbf{n}\right) \mathrm{d}A$ is the mass flow rate, which is approximately $8.0 \times 10^{-3}$ kg/s for the four cases. As shown by the dashed lines in Fig. 2, the mean bulk flow velocity is measured at the nozzle exit plane for the planar nozzle and the filleted orifice, while it is measured at the inlet plane for the square and bevelled orifices. These correspond to the region of minimum cross sectional area for each nozzle type. Defining the Reynolds number based on the mean bulk velocity is justified by the fact that this quantity is typically known, whereas the local velocity distribution is often unknown in practical engineering scenarios. This definition also facilitates meaningful comparisons between jets issuing from different nozzles operating under the same mass flow rate.

Prior to simulating the jet flow, a precursor simulation of a channel flow was conducted to generate time-varying inflow velocity data for the inlet boundary conditions of planar nozzle case, as shown in Fig. 2(a). Using a fully developed channel flow as the inlet boundary condition for the planar jet, as adopted in the experimental study of Sfeir[12], allows the exclusion of potential influences from the inlet velocity profile and turbulent intensity. The precursor simulation also enables the use of a shorter inlet section for the planar nozzle, thereby reducing the complexity and computational cost of the simulation. Prior to data collection, the precursor simulation was conducted for approximately 400 dimensionless time units,

$$t^* = \frac{tU_b}{h}, \tag{4}$$

where $t$ is physical time, $U_b$ is the bulk flow velocity of the jet and $h$ is the jet height. The turbulence statistics is shown in Appendix A. The collected time-varying velocity data was then assigned to the inlet boundaries of planar nozzle case using the OpenFOAM function `timeVaryingFixedValue`. Further details regarding this procedure can be found in He[3]. For the orifice cases, a normal velocity boundary condition with very low turbulence intensity ($< 1\%$) was prescribed at the inlet, which is consistent with the experimental studies of Deo et al.[16,18].

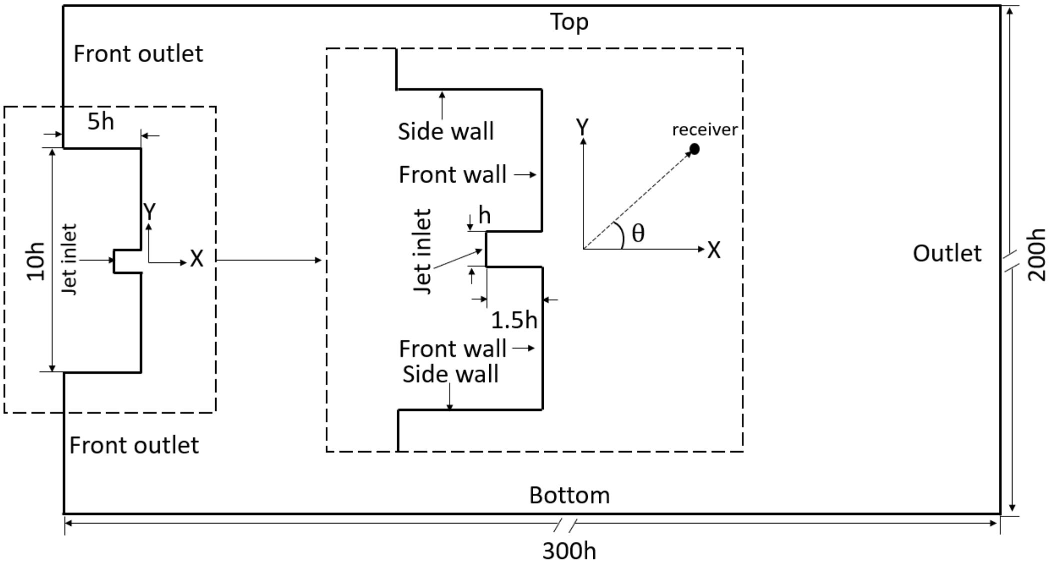

FIG. 3: Computational domain.

Pointwise v18.3 was utilized to generate a high-quality structured mesh for the computational domain. An example of the computational grid is illustrated in Fig. 4. As shown in Fig. 4(a), the refinement zone extends downstream of the jet up to $40h$, ensuring sufficient resolution in the region where the jet develops. In the transverse direction, the refinement zone spans approximately three times the width of the front wall, as depicted in Fig. 4(b). To increase the computational efficiency and minimize potential acoustic reflections from the domain boundaries, the mesh density is progressively coarsened outside of the core jet region. As shown in Fig. 4(b), within the FW-H integral surfaces (white dashed lines), the mesh resolution is maintained such that $\max(\Delta x, \Delta y) \leq 0.2h$. This mesh size provides a resolution of at least 20 points per wavelength up to a frequency of 20 kHz.

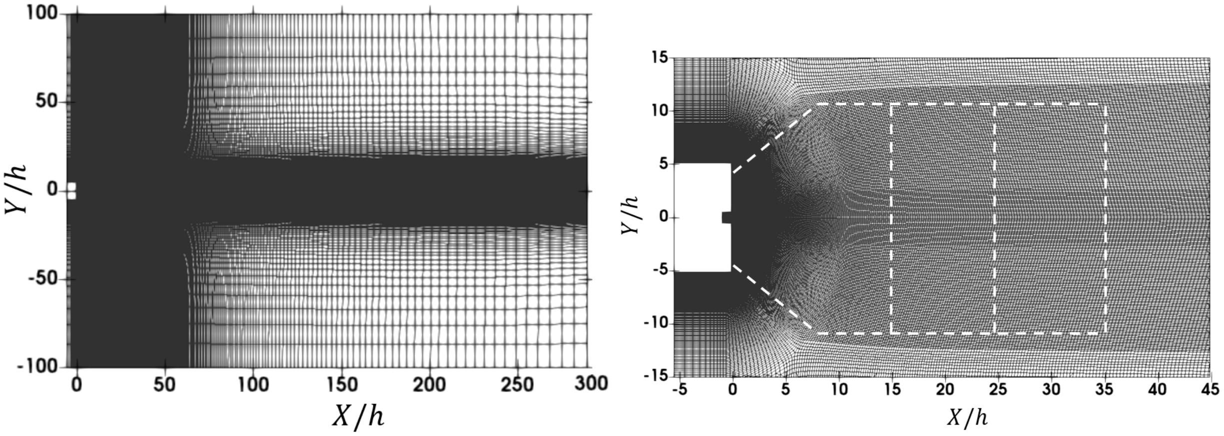

(a) (b)

FIG. 4: The mesh of type I exit in the X-Y plane. (a) overview of the mesh; (b) mesh in the vicinity of the jet nozzle.

Fig. 5 illustrates the mesh distribution for the four different types of nozzle geometries. A fine mesh is employed near the walls of the jet exits to accurately resolve the boundary layer. The expansion ratio of the boundary layer mesh is set to 1.1, and the first mesh node is positioned within the viscous sublayer to ensure $y^+ < 1$. Additionally, the mesh around the corners of the jet orifice lip is carefully refined to enhance grid quality and ensure high resolution of the flow development in this critical region.

The flow field simulations were conducted in OpenFOAM v2.4.0. The DDES method, as introduced in Section II A, coupled with the S-A turbulence model[33,39] was employed to solve the compressible N-S equations. The PIMPLE algorithm, a hybrid of PISO (Pressure Implicit with Splitting of Operators) and SIMPLE (Semi-Implicit Method for Pressure-Linked Equations), was utilized to solve the discretized equations. Prior to initiating the time resolved simulation, the

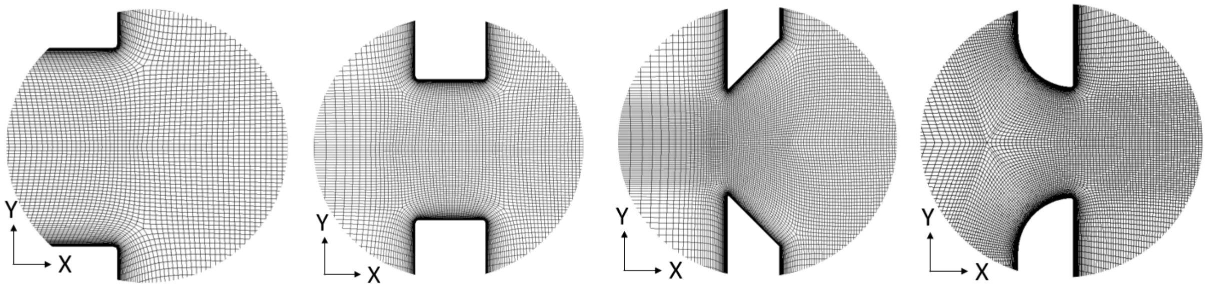

(a) (b) (c) (d)

FIG. 5: Details of the mesh for different types of exits. (a) Planar; (b) Square; (c) Bevelled; (d) Filleted.

initial flow field was obtained through Reynolds-Averaged Navier-Stokes (RANS) to provide an initial flowfield. For the unsteady simulation, a second-order implicit temporal scheme, specifically the “backward” time marching method, was adopted. The physical time step was set to $5 \times 10^{-7}$ seconds. This corresponds to a Courant–Friedrichs–Lewy (CFL) number between 0.5 and 1. For spatial discretization, a bounded second-order Total Variation Diminishing (TVD) scheme is employed. This scheme is commonly adopted in high-fidelity simulations to achieve a balance between numerical accuracy and solution stability and has been validated in numerical studies across a range of model scales[34,35].

### B. Grid resolution study and validation

The grid dependency study was conducted using the planar nozzle case with a spanwise length of $2h$ to reduce computational cost. Since the inlet velocity data is derived from a channel flow simulation, a long inlet section is not required. Therefore, the inlet length is set to only $1.5h$, as shown in Fig. 3. As shown in Fig. 4 and Fig. 5, the grid is finest near the nozzle exit. The size gradually increases in the transverse and streamwise directions. However, the grid size inside the integral surface (see Fig. 4(b)) maintains $\max(\Delta x, \Delta y) \leq 0.2h$. The details of the grid independence study cases are summarized in Table I. To maintain $y^+ < 1$, the first boundary layer grid height is set to $1.23 \times 10^{-3}h$. The mesh size is adjusted simultaneously along the solid surface and in the perpendicular direction. The aspect ratio of the baseline case was maintained at a constant value of 16, which is sufficiently small for both DDES and LES simulations[40]. The value of $\max(\Delta x, \Delta y)$ is taken within the region enclosed by the permeable FW-H surfaces, as highlighted in Fig. 4(b).

$N_{xy}$ denotes the number of cells in the X–Y plane and increases by approximately three times from the coarse mesh case (Coarse) to the fine mesh case (Fine). The primary changes in cell count occur downstream of the jet exit, while the number of cells in the spanwise direction remains constant across cases Baseline, Coarse, and Fine. To investigate the effect of spanwise resolution, additional cases (Spanwise-coarse and Spanwise-fine) were included, where the grid resolution in the spanwise direction was varied. This approach ensures a comprehensive evaluation of grid sensitivity while maintaining reasonable computational cost.

TABLE I: Grid parameters of the grid independence study.

| Case | $\Delta x/\Delta y$ | $\max(\Delta x, \Delta y)/h$ | $\Delta z/h$ | $N_{xy}$ |
|---|---|---|---|---|
| Baseline | 16 | 0.2 | 0.2 | $1.31 \times 10^5$ |
| Coarse | 32 | 0.4 | 0.2 | $0.86 \times 10^5$ |
| Fine | 8 | 0.1 | 0.2 | $2.56 \times 10^5$ |
| Spanwise-coarse | 16 | 0.2 | 0.33 | $1.31 \times 10^5$ |
| Spanwise-fine | 16 | 0.2 | 0.1 | $1.31 \times 10^5$ |

Fig. 6 presents the time-averaged velocity profiles along the centreline and in the transverse direction. $U_{\mathrm{cl}}$ is the mean streamwise velocity at the centreline. It is observed that the centreline velocity profiles for all cases (Fig. 6(a)), except for the Spanwise-coarse case, exhibit good agreement with each other. The deviations at each monitor between the numerical results and the experimental data are all less than 3%, except for the Spanwise-coarse case, which shows a difference of approximately 8% from $30h$ to $60h$. A similar trend is also noted for the mean velocity profiles in the transverse direction (Fig. 6(b)). $\eta$ is defined as the varying dimensionless transverse position ($Y/X_{\mathrm{cl}}$, where $X_{\mathrm{cl}}$ is the streamwise position of the transverse line). The discrepancy observed in the spanwise-coarse case, up to 40%, highlights the critical importance of the spanwise grid resolution for accurately simulating jet flow. Apart from this discrepancy with inadequate spanwise resolution, the simulated centreline and transverse velocity profiles agree well with the experimental data from Deo et al.[16] and Sfeir[12]. Therefore, based on the above comparisons, the grid parameters from the baseline case are employed in the subsequent simulations.

As mentioned earlier, a periodic boundary condition is applied in the spanwise direction of the simulation domain. To justify an adequate spanwise length of the simulations, the spanwise cor-

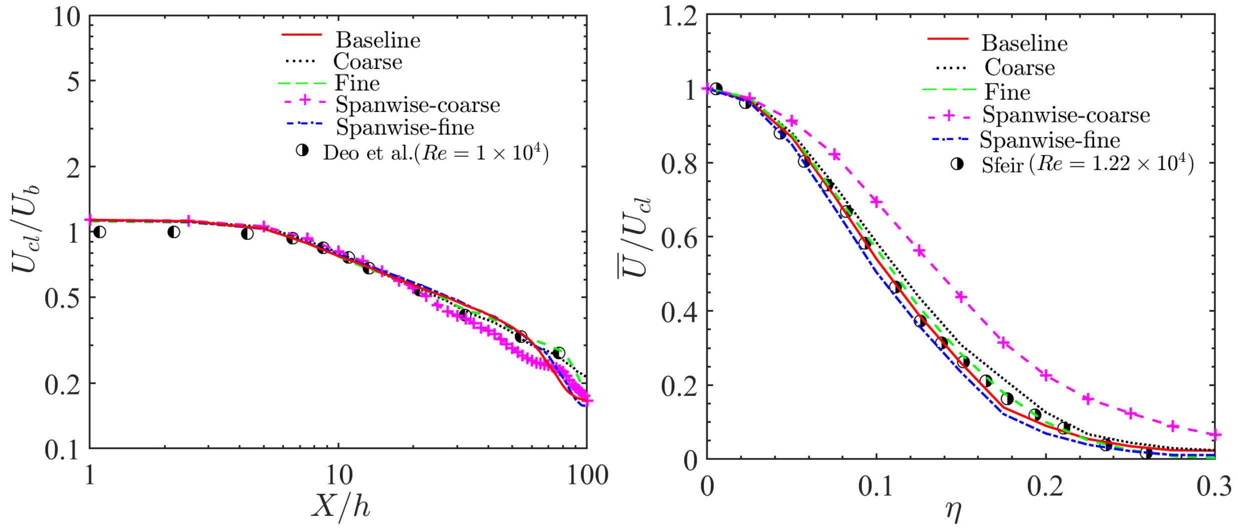

(a)

(b)

FIG. 6: Mean velocity profiles. (a) Streamwise direction. The experimental data is from Deo et al.[16] (b) Transverse direction at x=30h. The experimental data is from Sfeir[12].

relation coefficients were calculated for four cases with spanwise lengths of $2h$, $5h$, $10h$, and $15h$, as shown in Appendix B. To balance accuracy in capturing the spanwise variations and the computational cost, the case with a spanwise length of $10h$ was chosen for the subsequent simulations. Therefore, the subsequent validation is performed based on the simulation case with a spanwise domain width of $10h$. In the simulation, the flow field becomes stable after a dimensionless time $t^*$ (defined in Eq. (4)) of approximately $10^3$. The data sampling is then performed over the same time duration again. The total computational wall time for this process was approximately 150 hours, utilizing 320 cores on Intel Xeon Gold 6138 processors on the Iridis5 cluster at the University of Southampton.

The examination of self-similarity behaviour is illustrated in Fig. 7. In Fig. 7(a), the fitted mean transverse velocity profile from Sfeir[12] is used as a reference. The numerical results show excellent agreement with the experimental data. Additionally, the numerical results also demonstrate strong self-similarity between the velocity profiles at different positions ($10 < X/h < 50$), indicating that the flow exhibits consistent scaling behaviour in this region. This self-similarity is a characteristic feature of fully developed turbulent jets. In Fig. 7(b), the streamwise turbulence intensity ($U'/U_{cl}$) along the transverse direction is compared, where $U'$ is the root mean square of the streamwise velocity. The streamwise turbulence intensity also shows a good agreement with the experimental data.

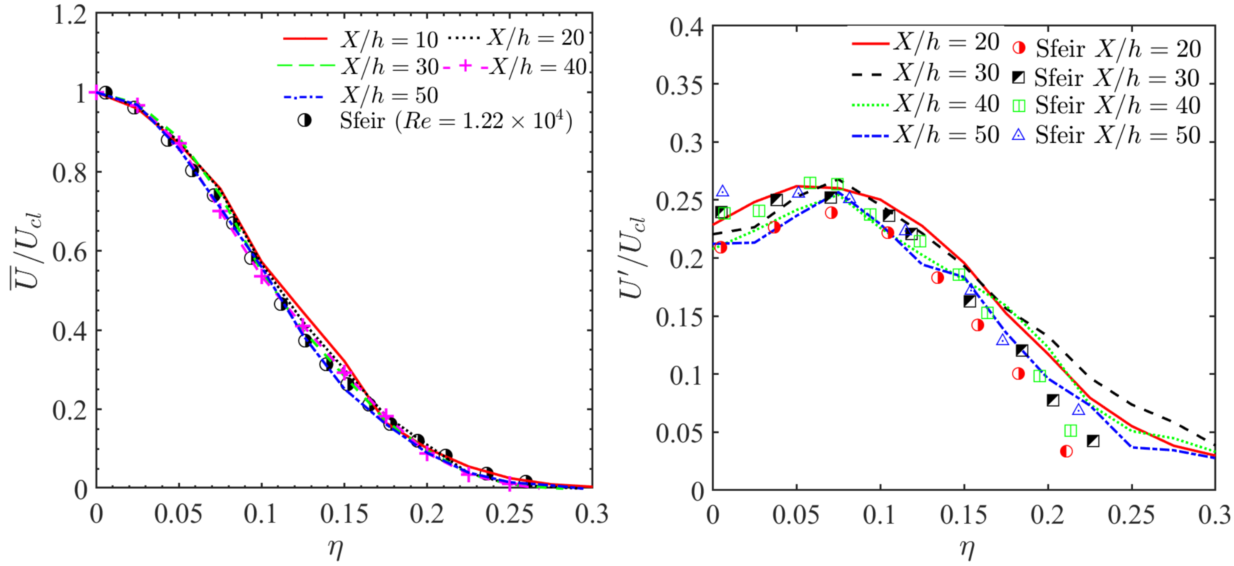

(a) (b)

FIG. 7: Dimensionless velocity profile in the transverse direction. (a) mean velocity profiles; (b) turbulent intensity in the streamwise direction. The experimental data is from Sfeir[12].

To optimize the placement of the FW-H permeable integral surface, three different locations, as shown in Fig. 4(b), are tested to determine the most effective position for accurately capturing the jet noise. The integral surfaces, shown alongside with the the divergence of velocity derivative and the normalized Q criterion ($Qh^2/U_b^2$), are shown in Fig. 23 in Appendix B. The results, presented in Fig. 24 in Appendix B, show that the noise spectra converge with the placement of the integral surfaces for the two largest integral surfaces. The largest of the integral surfaces was chosen for the acoustic analysis as it encloses a larger portion of the jet.

To validate the acoustic simulation, a jet configuration matching the experimental conditions (listed in Table II) is simulated. The jet height matches the experimental setup, while the spanwise length is reduced to 10 mm to decrease computational costs. Periodic boundary conditions are used in the spanwise direction. Grid parameters, such as the aspect ratio and mesh distribution, are kept consistent with the baseline case in Table I. However, other parameters including the height of the first boundary layer mesh and the volume mesh resolution are refined because the jet velocity increases to 149 m/s. The total grid count for the validation simulation is approximately 27 million cells. All flow conditions match those used in the experiment conducted by Munro and Ahuja[41].

TABLE II: Jet parameters for the current acoustic validation simulation and the experiment by Munro and Ahuja[41].

| | Acoustic Validation Sim. | Munro and Ahuja[41] |
|---|---|---|
| $U_b$ (m/s) | 149 | 149 |
| $h$ (mm) | 1 | 1 |
| $w$ (mm) | 10 | 375 |

Fig. 8 compares the simulated noise spectra of the acoustic validation case with experimental data from Munro and Ahuja[41]. In the comparison, the numerical result is scaled to account for the difference in spanwise width with the experimental setup previously discussed using following equation,

$$\Delta \mathrm{SPL} = 10\log_{10}\left(\frac{w_1}{w_2}\right), \tag{5}$$

where $w_1$ is the nozzle width in the acoustic validation simulation case and $w_2$ is the nozzle width in the experiment by Munro and Ahuja[41]. A reasonably good agreement is observed between the simulation and experimental acoustic data, despite in general some over-prediction across most frequencies. This discrepancy can be attributed to two main factors. One is the use of periodic boundary conditions in the spanwise direction in the simulation. This neglects end effects, which are present in the experiment. The second is the absence of width consideration in the frequency scaling. Nevertheless, despite these approximations, the overall agreement supports the validity of the numerical simulation setup.

## IV. RESULTS AND DISCUSSION

### A. Flow field

Based on the streamwise velocity decay, a rectangular jet flow can be divided into three regions. The first is the potential core region, where the streamwise velocity is essentially constant. The second is the two-dimensional region, where turbulence increases and self-similarity begins. The third region is where the flow becomes fully developed and turbulence becomes more homogeneous and isotropic in nature, with large-scale turbulent structures dominating the dynamics[42]. This region is analogous to the axisymmetric region in a circular jet. Experimental research has

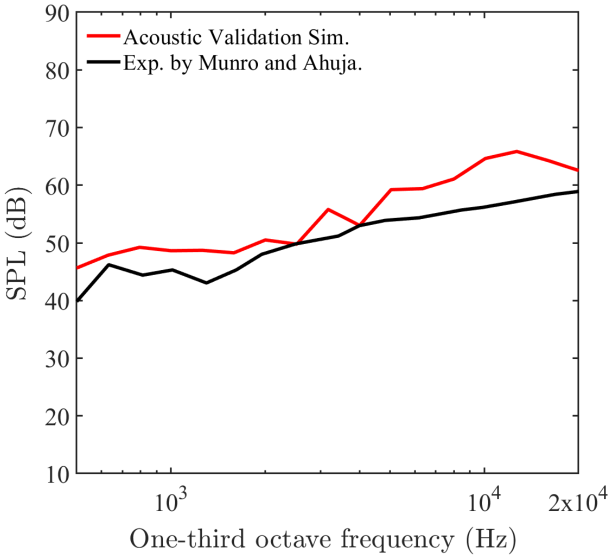

FIG. 8: Validation of the aeroacoustic simulation at an angle of 60° and a radial distance of 2.74 m. The experimental data is from Munro and Ahuja[41].

demonstrated that the influence of nozzle geometries is most pronounced in the vicinity of the nozzle exit (potential core region and two-dimensional region), while the effects tend to diminish and the flow becomes self-similar further downstream[11,12,18].

The normalized mean velocity magnitude ($\overline{U}_a/U_b$) near the potential core region is presented in Fig. 9. $\overline{U}_a$ is the time-averaged magnitude of the velocity defined as $\overline{U}_a = \sqrt{\overline{U}^2+\overline{V}^2+\overline{W}^2}$. The potential core length ($x_p$) is defined as the distance from the jet exit to the point on the centreline where $\overline{U} = \overline{U}_{\text{exit}}$, and $\overline{U}$ is the mean streamwise velocity. The potential core regions are highlighted by the solid white lines and the jet half-width are highlighted by the black dashed lines. The jet half-width ($y_{0.5}$) is defined as the transverse distance from the jet centreline to the point where $\overline{U} = 0.5U_{\text{cl}}$. In Fig. 9(a), the flow velocity at the exit of the planar nozzle is relatively uniform within the first nozzle height region and initially remains unexpanded within the potential core region. This behaviour is similar to the filleted orifice. For both the square and bevelled orifices, both of which have a sharp-edge at the exit, there is a vena contraction as highlighted by the white arrow in Fig. 9(b) and (c). The vena contraction forms just downstream of the sharp edge due to the transverse velocity component developed near the orifice wall. As the flow is forced through the orifice, it abruptly redirects streamwise, but the transverse momentum persists, leading to flow contraction and acceleration. Consequently, the jet velocity is higher in these cases compared to the planar nozzle. This phenomenon was also reported in the experimental studies from Deo et al.[18] and Quinn[13].

The filleted nozzle also demonstrates a vena contraction (Fig. 9(d)), although it is much weaker than the vena contraction seen in the square and bevelled orifices (Fig. 9(b) and (c)). This can be attributed to the presence of the fillet, which gradually directs the flow in the streamwise direction. Unlike the sharp-edged nozzles, where the transverse momentum is abruptly redirected, the contraction in the filleted nozzle facilitates a smoother and more gradual re-orientation of transverse momentum to streamwise momentum. Therefore, the flow velocity along the centreline at ($x/h$= 0) is lower than that observed in the square and bevelled orifices, resulting in a longer potential core length ($x_p/h$= 7.5) compared to those two cases.

Fig. 10 illustrates the normalized mean streamwise velocity $U_{cl}/U_b$ and streamwise turbulence intensity $U'/U_b$ along the centre line in the $X$-$Y$ plane. The mean velocity profiles (Fig. 10(a)) of the planar nozzle and the filleted orifice are quite similar, while the square and bevelled orifices are similar to each other. The mean velocity profiles of the square and bevelled orifices are significantly higher than the other two cases, especially near the nozzle exit. As illustrated in Fig. 9, this increase results from the vena contraction effect induced by the sharp-edged nozzle, which accelerates the flow due to a reduction in effective flow area. The velocity ratio reaches its maximum at one nozzle height downstream and then decreases. In contrast, the profile of the filleted orifice reduces this acceleration effect, having only a small velocity increase immediately after the exit, followed by a relative constant velocity until $X/h = 3$, whereafter it decreases in a similar manner to the planar nozzle.

The streamwise turbulent intensity ($U'/U_{cl}$) is shown in Fig. 10(b). The planar nozzle has a similar trend, albeit slightly higher, compared to filleted orifice up to $X = 14h$. The slight increase in turbulence intensity at the exit of the planar nozzle ($X = 0$), compared to the filleted orifice, is due to the fully developed inlet boundary condition of the planar nozzle, which results in greater turbulence intensity at the nozzle exit. For both the square and bevelled orifices, significantly higher turbulence intensity levels are observed compared to the other two cases, extending downstream to $X = 20h$. Their sharp edges accelerate the flow through a vena contraction. This increase in velocity, increases the velocity gradients and strain rates, thereby increasing the turbulence intensity. This is consistent with findings from the experimental research by Deo et al.[18]. Their study also demonstrated a consistent dependence of streamwise turbulence intensity on the fillet radius, with the highest turbulence intensity occurring with no fillet present, i.e. a sharp-edge case. In this present work by comparing directly the four different nozzle types, it is shown that the

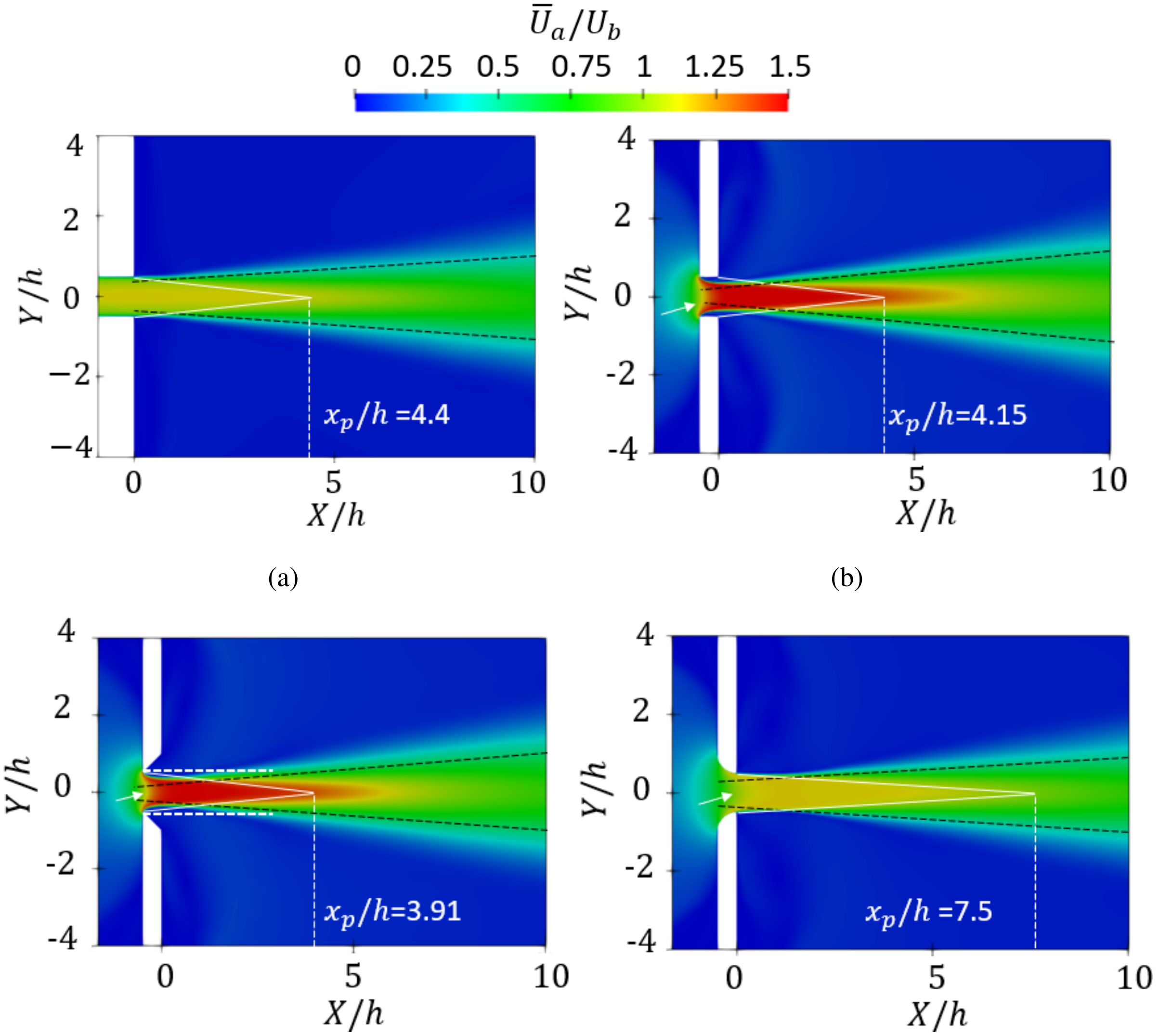

(a) (b)

(c) (d)

FIG. 9: The normalized time-averaged velocity magnitude $\overline{U}_a/U_b$ contour in the vicinity of different nozzle exits, (a) Planar nozzle; (b) Square nozzle; (c) Bevelled-edge nozzle; (d) Filleted-edge nozzle. The black dashed lines denote the jet half-width and the solid white lines denote the potential core. The white arrow indicates the vena contraction.

square-edge case exhibits similar near-field turbulence statistics to the bevelled-edge case, while the planar nozzle closely resembles the filleted-edge case.

Fig. 11 presents the near-field streamwise velocity profiles in the transverse direction at a streamwise positions $X/h = 4$ and 8. At $X/h = 4$ (Fig. 11(a)), the values of $\overline{U}/U_{cl}$ for the square and bevelled orifices in the transverse direction are lower than the other two cases for values of $\eta$ below 0.2. However, further downstream at $X/h = 8$ (Fig. 11(c)), the mean velocity becomes

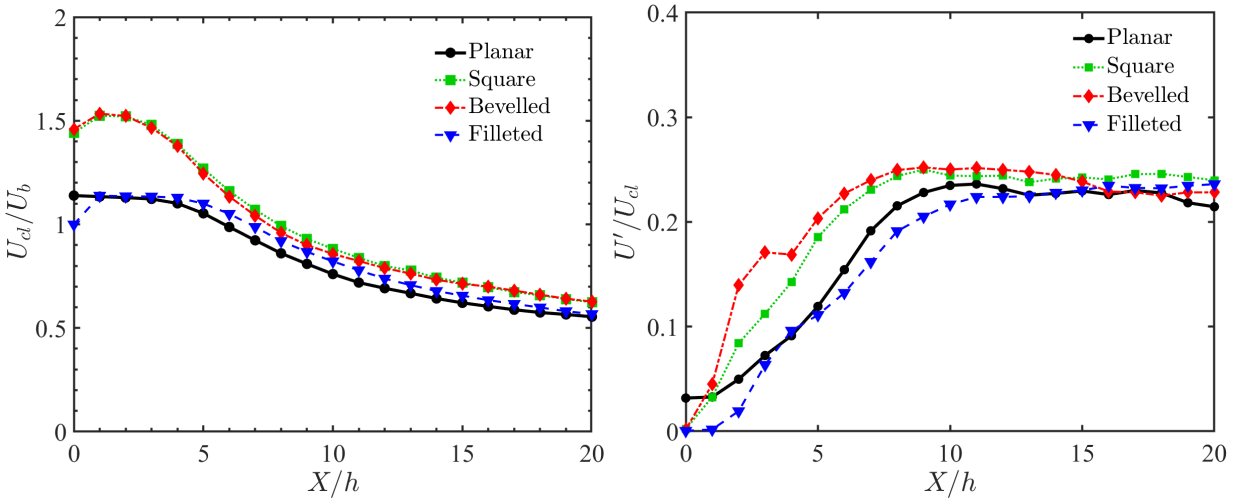

(a)

(b)

FIG. 10: Near-field evolution of the centreline velocity, (a) normalized streamwise mean velocity; (b) normalized streamwise turbulence intensity.

greater because of the rapid decay of the centreline velocity $U_{cl}$. This behaviour is attributed to the vena contraction effect of the sharp-edge cases, which exhibit significantly higher centreline velocity ($U_{cl}$) than the planar or filleted cases at $X/h < 5$. Further downstream, this difference becomes less and the centreline velocities converge as previously shown in Fig. 10(a).

Near the end of the potential core at $X/h = 4$ (Fig. 11(b)), the turbulence intensity peak appears closer to the centreline for the sharp-edge cases ($\eta \approx 0.1$) compared to the planar nozzle and filleted orifice ($\eta \approx 0.15$). This shift in traverse location can also be attributed to the vena contraction resulting in a higher velocity gradient near the potential core. Further downstream at $X/h = 8$ (Fig. 11(d)), the transverse positions of turbulent intensity peaks of all cases are closer to the centreline ($\eta \approx 0.075$). The reduction in transverse positions of the peaks is due to the downstream spreading and mixing of the shear layer, which makes the turbulence intensity higher near the centreline. In both Fig. 11(b) and (d), the square and bevelled orifices exhibit consistently higher turbulent intensity values in the transverse profiles. This indicates that the sharp edge produces a stronger shear layer than the other two types of inlet nozzle due to the vena contraction.

The normalized instantaneous vorticity magnitudes ($\omega h/U_b$) of four cases in the mid $Z$ plane are shown in Fig. 12. Only the near field of the nozzle is presented, as the low velocity secondary flows on the outside walls of the nozzle caused by flow entrained by the jet are not of interest and only have a limited influence on the overall jet development. The vorticity magnitude ($\omega$) is

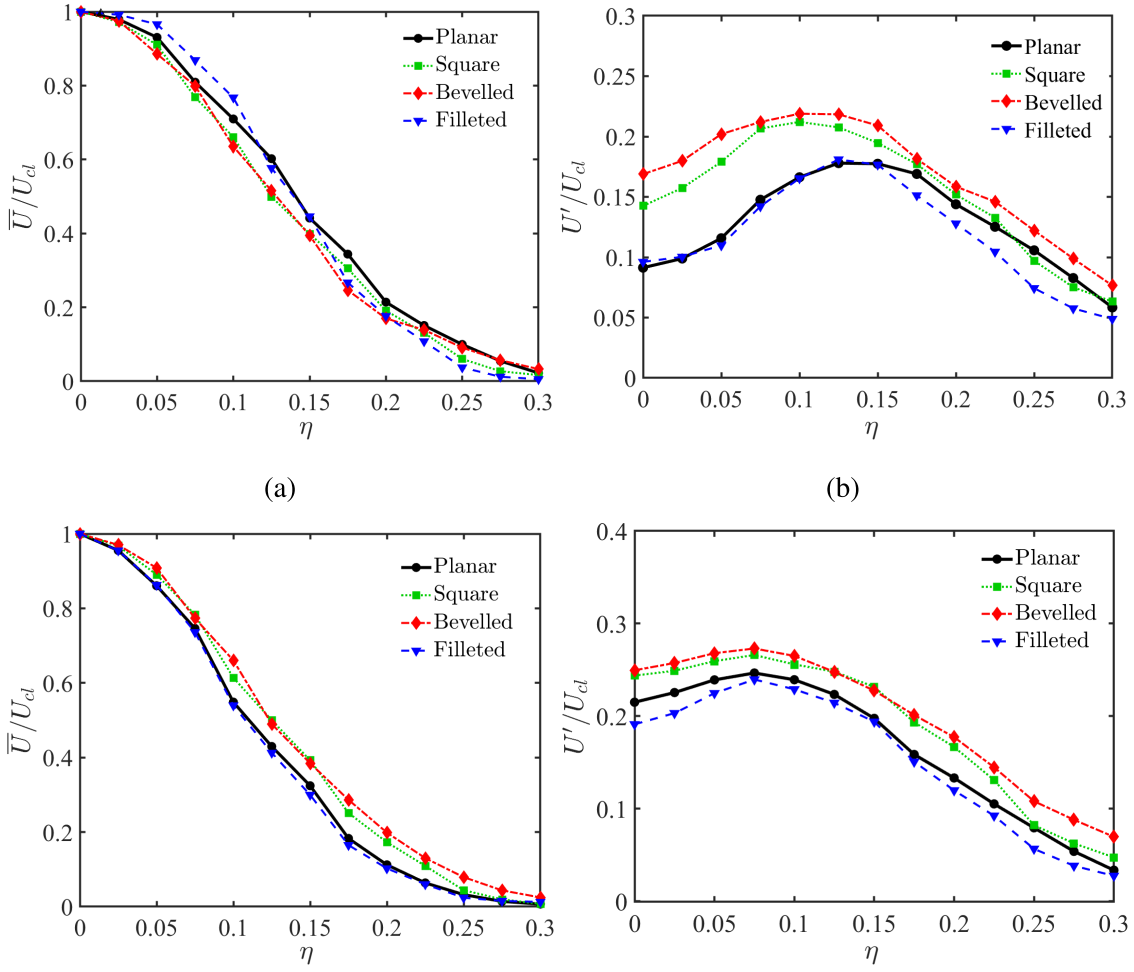

(a) (b)

(c) (d)

FIG. 11: Near-field streamwise velocity statistics in the transverse direction. (a) normalized streamwise mean velocity at $X/h = 4$; (b) normalized streamwise turbulence intensity at $X/h = 4$. (c) normalized streamwise mean velocity at $X/h = 8$; (d) normalized streamwise turbulence intensity at $X/h = 8$.

calculated as:

$$\omega = \sqrt{\left(\frac{\partial W}{\partial Y} - \frac{\partial V}{\partial Z}\right)^2 + \left(\frac{\partial U}{\partial Z} - \frac{\partial W}{\partial X}\right)^2 + \left(\frac{\partial V}{\partial X} - \frac{\partial U}{\partial Y}\right)^2} \tag{6}$$

where $(U,V,W)$ is the velocity vector. When the flow separates from the edges of the jet nozzle, a free shear layer forms due to the velocity difference between the jet and the surrounding ambient fluid, resulting in a strong velocity gradient. Downstream of the nozzle exit, small perturbations arise within this shear layer. These perturbations initiate the development of Kelvin–Helmholtz instabilities, which generate a roll-up of the shear layer and emergence of coherent vortical structures as shown in Fig. 12. The shear layer initially undergoes a consistent growth in thickness characterized by the relatively orderly roll-up of the vortices. The vortex size increases as they convect downstream. As they increase in size, this leads to increased vortex interactions, breakdown of coherent vortices, and the onset of enhanced turbulent mixing near the end of the potential core[43]. Therefore, towards the end of the potential core region, the shear layer becomes increasingly unsteady.

This observed process of vortex formation and breakdown is consistent with the findings in study by Ghasemi[44] and Nekkanti et al.[45] (although observed for different nozzle types and flow conditions). As shown previously in Fig. 9, the velocity ratio $\overline{U}_a/U_b$ near the exit of sharp-edge cases are close to 1.5, resulting in a larger velocity gradient compared to the other two cases. This larger velocity gradient generates greater strain rates and causes earlier vortex roll-up in the shear layer (Fig. 12(b) and (c)) compared to the planar nozzle and filleted orifice shear layer (Fig. 12(a) and (d) respectively). Near the end of the potential core, the rolled-up vortices in the shear layer penetrate the boundary of the potential core and even extend beyond the centreline of the jet. Therefore, there is a strong interaction between both shear layers as the streamwise distance increases from the jet exit. This phenomenon is more significant for the sharp-edge orifices (square and bevelled orifice) than for the other two cases. The vortex emergence position in the shear layer of the filleted orifice is delayed and is extended to approximately $X/h = 2$, as shown in Fig. 12(d). This is the longest of the four cases. This is because the filleted nozzle, with its curvature guiding the flow through the orifice exit, results in smaller velocity gradients and lower turbulence intensity in the shear layer immediately downstream of the nozzle, thereby delaying the onset of Kelvin–Helmholtz instabilities and vortex roll-up.

To quantify the jet spreading and decay, the similarity relationship for a plane jet is investigated by the following equations:

$$\left(\frac{U_b}{U_{cl}}\right)^2 = C_{1u}\left(\frac{X}{h} + C_{2u}\right), \tag{7}$$

$$\frac{y_{0.5}}{h} = K_{1u}\left(\frac{X}{h} + K_{2u}\right), \tag{8}$$

where $X$ is the streamwise location, $y_{0.5}$ is the jet half-width, and $C_{2u}$ and $K_{2u}$ are the virtual origins. $C_{1u}$ is the slope of $(U_b/U_{cl})^2$, which indicates the decay rate of the centreline velocity $U_{cl}$. $K_{1u}$ is the spreading rate, which describes the decay of streamwise velocity ($\overline{U}$) in the transverse direction. $C_{1u}$ and $K_{1u}$ are both determined by the streamwise velocity at $x/h = 10$ and $x/h = 20$.

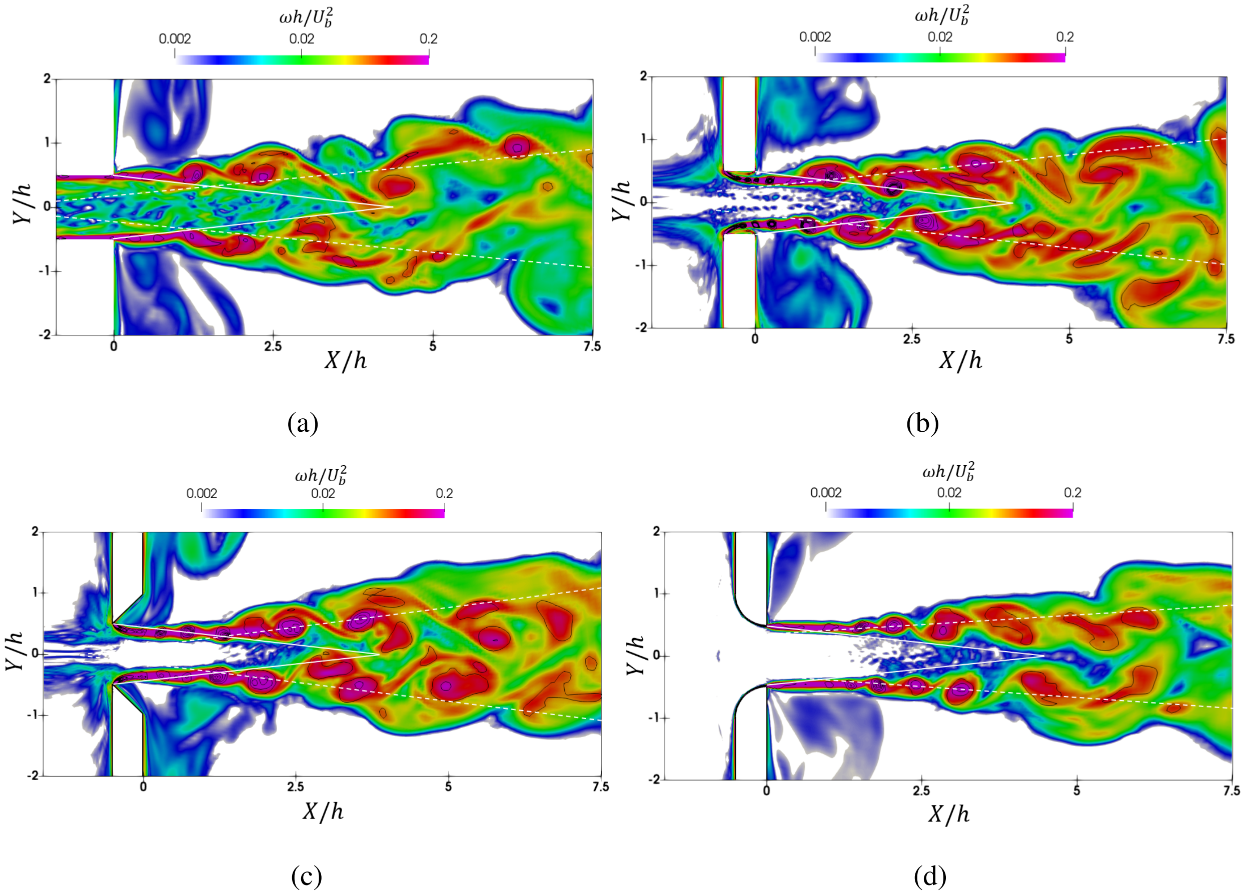

(a)

(b)

(c)

(d)

FIG. 12: Visualization of instantaneous normalized vorticity magnitude in the shear layer in the X-Y plane at the mid-span; the contour is vorticity and the vortex is visualized by normalized Q-criterion ($Qh^2/U_b^2$) which ranges from 1 to 50; (a) Planar nozzle; (b) Square nozzle; (c) Bevelled-edge nozzle; (d) Filleted-edge nozzle. The dashed lines denote the $y_{0.5}$, the solid lines denote the potential core.

Table III summarizes the centreline velocity decay and spread ratio for different nozzle types. For reference, it also includes values from previous research from Matsuyama[22] and Deo et al.[16]. The decay rate ($C_{1u}$) of the planar nozzle is similar to the numerical results of a planar jet reported by Matsuyama[22]. The difference is approximately 6%. Meanwhile, the $C_{1u}$ value for the filleted-edge case is similar with the experimental result of a filleted nozzle from Deo et al.[16], differing by approximately 4.6%.

Comparing the four different nozzle types in Table III, the decay rate $C_{1u}$ of the planar nozzle and filleted orifice are similar, while the square and bevelled orifices have lower values, which indicates a slower decay of centre velocity ratio. An explanation for this is that the vena contraction effect, previously identified, increases the exit velocity in both the sharp-edged cases. This causes the velocity on the centreline to decay over a longer distance to the same velocity compared to the other two cases (planar nozzle and filleted orifice) without the strong vena contraction. For the spreading rate $K_{1u}$, the difference between the current result for the planar case and that reported by Matsuyama[22] is 13.6%, while the difference for the filleted nozzle with experiment from Deo et al.[16] is 16%. Again, comparing the four different nozzle types, the planar nozzle has the smallest value of spreading rate while the square orifice has the largest. The difference between the planar nozzle and the square orifice spreading rate is approximate 18%.

Fig. 13 presents the streamwise evolution of dimensionless jet half-width ($y_{0.5}/h$) in the nearfield. For $X/h < 4$, both the square and bevelled orifices have smaller $y_{0.5}/h$ values because of the vena contraction effect, as illustrated in Fig. 9(b) and (c). However, it increases more rapidly than the planar nozzle for $X/h > 4$. This rapid increase in jet half-width results in higher spreading rates in the near field of the jet nozzle for $X/h < 10$. This enhanced spreading is attributed to greater turbulence intensity and mixing in the shear layer at the edge of the potential core, as shown previously in Fig. 11 and Fig. 12, which promotes greater momentum transfer between the jet and the surrounding quiescent fluid.

TABLE III: Summary of velocity decay ($C_{1u}$) and jet spreading rates ($K_{1u}$) for the four different nozzle types in the current simulations. The experimental data from Matsuyama[22] is a planar nozzle. The experimental data from Deo et al.[16] is a filleted nozzle.

| | Sim.<br>Planar | Sim.<br>Square | Sim.<br>Bevelled | Sim.<br>Filleted | Matsuyama[22]<br>Planar | Deo et al.[16]<br>Filleted |
|---|---|---|---|---|---|---|
| $C_{1u}$ | 0.163 | 0.129 | 0.118 | 0.164 | 0.153 | 0.172 |
| $K_{1u}$ | 0.100 | 0.118 | 0.113 | 0.116 | 0.088 | 0.100 |

### B. Jet dynamics

To investigate the time-dependent behaviour of the shear layer, a monitor was positioned at $2h$ on the lip line within the shear layer to analyse periodic features in the turbulent velocity spectrum. The power spectral density (PSD) of the streamwise velocity at this location is shown in Fig. 14. For the planar nozzle, as shown in Fig. 14(a), the PSD reveals broadband humps centred around

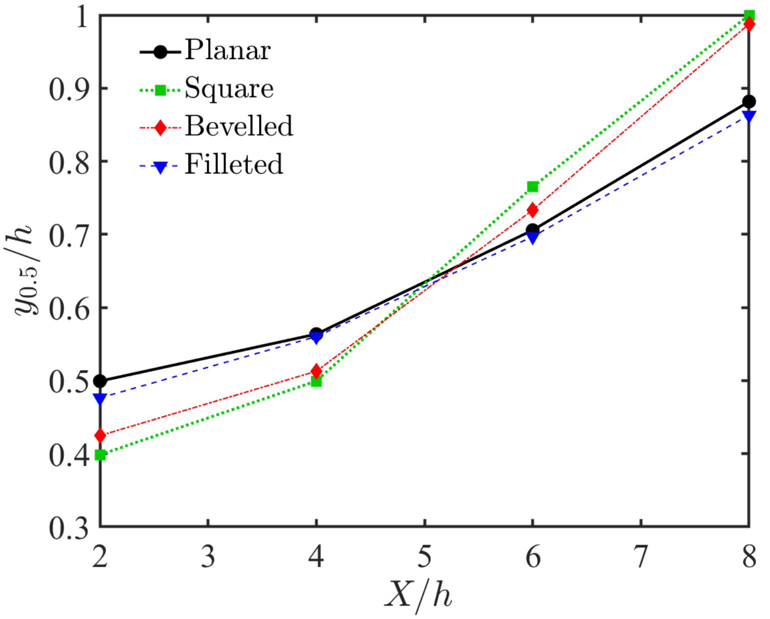

FIG. 13: Streamwise evolution of the jet half-width for different nozzle profiles.

approximately 3.3 kHz, whereas the filleted orifice exhibits a more distinctive hump at 5.2 kHz. In Fig. 14(b), the spectrum of the square orifice case exhibits a broadband spectrum, except for small peaks at frequencies of approximately 8.5 kHz and 12.7 kHz. In contrast, the spectrum of the bevelled orifice exhibits prominent peaks at 4.3 kHz, 8.5 kHz, 12.7 kHz, and 16.9kHz, with significantly higher amplitudes compared to the other three cases. The first peak corresponds to the fundamental vortex roll up frequency in the jet shear layer, while the subsequent peaks represent its harmonics. The amplitudes of these harmonics are significantly lower than that of the fundamental frequency. Therefore, only the fundamental, second and third harmonics are analyzed further. It was previously shown that the bevelled orifice case had the highest velocity gradient, resulting from the increased centreline velocity due to the strong vena contraction effect (shown in Fig. 9). This generates a shear layer for this case with larger values of vorticity (shown in Fig. 12). For this particular nozzle geometry, the amplitudes of the peaks are more pronounced compared to other cases. These tonal features align with the vortex structures depicted in Fig. 12, highlighting the direct relationship between shear layer dynamics and the spectral characteristics of the velocity. The significance of the prominent peaks in the bevelled case arises from the vortex motion and the interactions between the vortices in the shear layers, which will be discussed in the following section.

SPOD is a powerful technique for analysing coherent flow structures in the frequency domain

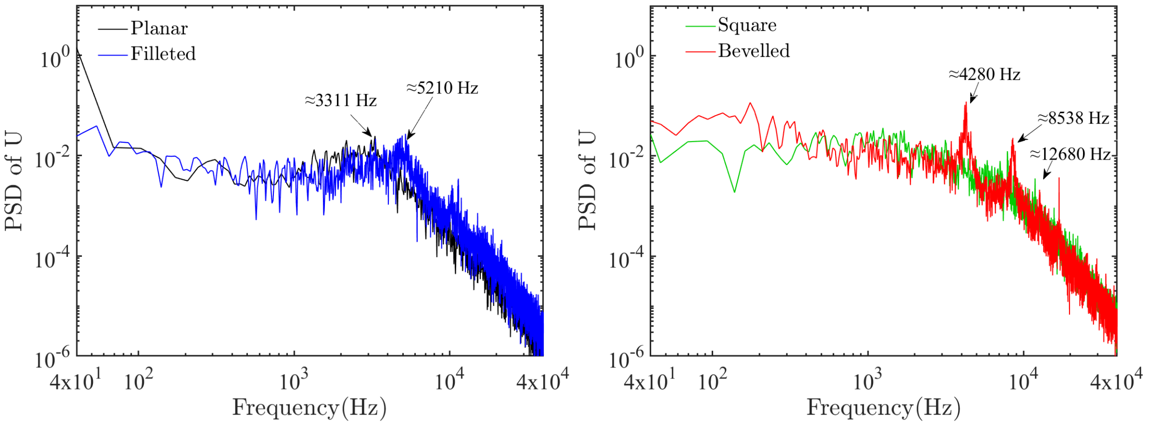

(a)

(b)

FIG. 14: PSD of the streamwise velocity. (a) Planar nozzle and filleted orifice; (b) Square and bevelled orifices.

and their underlying dynamics. Originally proposed by Lumley[46], it has since been further developed and applied to study dynamics in flows[43,47–49]. SPOD allows for the extraction of dominant coherent structures and dynamic modes in complex turbulent flows, providing insight into both the spectral characteristics and spatially coherent structures. In this study, SPOD is employed to identify the flow structures most responsible for the generation of tonal peaks in the bevelled orifice jet and to determine the spatial regions that contain these modes. To investigate the relationship between the pronounced tonal peaks in the bevelled orifice and the vortices in its shear layer, SPOD is used to visualize the coherent structures in the flow field.

Fig. 15 shows the first and second modes of the fundamental frequency (4.3 kHz) and its harmonics (8.6 kHz and 12.9 kHz) for the bevelled orifice. A dimensionless time length (Eq. (4), $t^* = tU_b/h$) of 500 of the pressure field is sampled for the calculation of SPOD. Such a length of sampling is crucial in identifying dominant modes, particularly in turbulent flows where both time and spatial coherence are significant. As shown in Fig. 15, the instability at 4.3 kHz concentrates towards the rear half of the potential core (from $1.6h$ to $4h$) and it is the most energic in both modes 1 and 2. This region closely corresponds to the area where the vortices in the shear have grown to sufficient size that interactions between the two shear layers occur (see Fig. 12(c)). Therefore, the peaks observed in the turbulent velocity spectrum of the bevelled orifice, as shown in Fig. 14(b), are strongly associated with vortex behaviour in the free shear layers downstream of the jet exit.

Similar SPOD modes are observed in the other three cases, though not shown here due to space limitations. These modes all reflect vortex dynamics within the shear layer. The same mechanism applies. However, the associated modes of spectral peaks and humps exhibit lower amplitudes compared to the bevelled case. The peaks and humps in the spectra are closely associated with periodic phenomena such as vortex roll-up and vortex interaction between both shear layers. The more pronounced peaks observed in the spectra for the bevelled orifice are likely attributed to the stronger shear layers generated by the vena contraction effect, which are also closer together due to the strong vena contraction effect (see Fig. 12). This results in stronger interactions compared to the other cases.

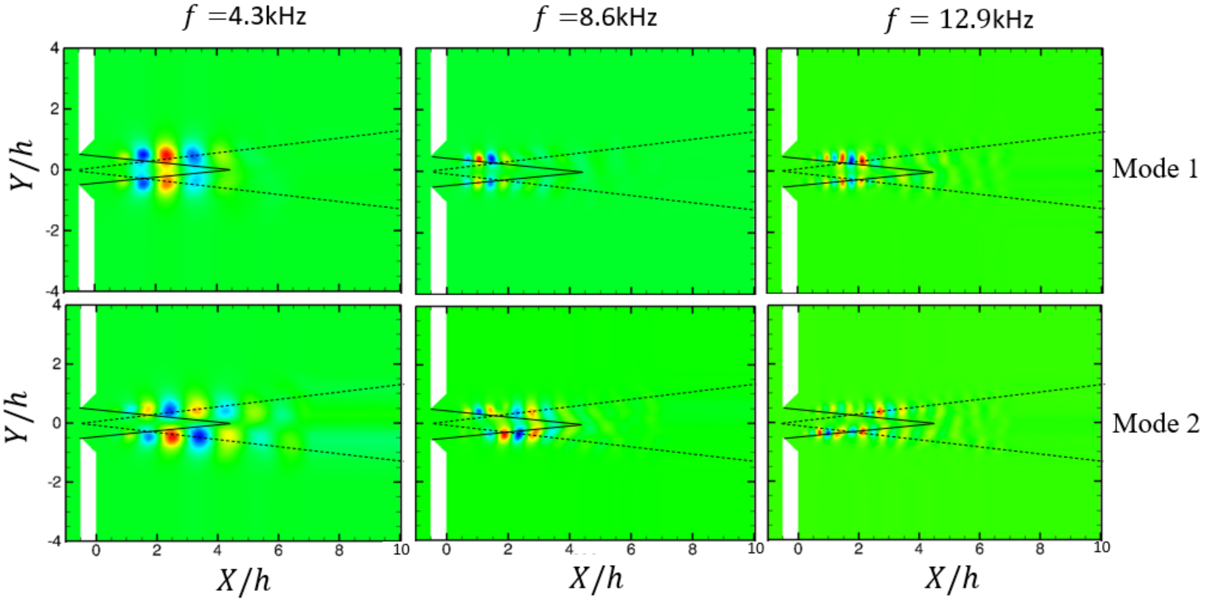

FIG. 15: SPOD modes of the bevelled orifice case. The solid black line is potential core boundary, while the dash black line is the jet half-width ($y = y_{0.5}$).

Fig. 16 illustrates the instantaneous vorticity field of the bevelled case at four different instants in time. The dimensionless time interval is defined as $\Delta t^* = \Delta t U_b/h$, where $\Delta t$ is the physical time difference. The first snapshot corresponds to $t = 0.327$ s. As highlighted by the white arrows, the transverse distance between the vortices in both shear layers of the bevelled nozzle at $X = 2h$ periodically reaches a minimum. The time duration of this process is $\Delta t^* = 2.4$. The vortices from both shear layers appear almost simultaneously at $X = 2h$, which explains this periodic reduction in distance due to their synchronized motion. Such in-phase vortex motion is observed only in the bevelled case, even though the square case exhibits a similar configuration and comparable turbulence statistics near the nozzle, as shown in Fig. 10 and Fig. 11. This difference is likely attributable to the different flow interactions governing the early stage of vortex formation in the bevelled nozzle, compared to the more complex vortex roll-up dynamics present in the square nozzle, as shown in Fig. 12.

The frequency of this periodic vortex interaction can be estimated from the instantaneous vorticity field at different times to be 4.2 kHz, very close to the peak frequency observed in Fig. 14(b). Furthermore, the SPOD results in Fig. 15 show that the most energetic vortical structures occur at 4.3 kHz, indicating that the interaction frequency matches the dominant frequency of vortex interaction in this region. Although a similar vortex frequency is present in the square nozzle case, no consistent in-phase vortex motion is found. This explains why the peaks in Fig. 14(b) for the square case are weaker than those in the bevelled case. The pronounced peaks observed in the the streamwise turbulent velocity spectrum in the bevelled nozzle case can be attributed to several interacting factors. First, the shear layer strength is enhanced due to the vena contraction effect. Second, the spacing between the upper and lower shear layers is reduced, which is also a result of the vena contraction. Finally, the sharp edge of the bevelled nozzle promotes simultaneous vortex roll-up and shedding from both shear layers that are crucially in phase with each other. These combined effects contribute to the strong tones seen in the turbulent velocity spectrum.

Based on the above analysis, the tonal peaks in the spectra of square and bevelled nozzles arise from vortex interactions between the two shear layers at the nozzle lips, which is enhanced by their sharp edges. This explains why the planar and filleted nozzles, despite generating vortex roll-up in the detached shear layers, exhibit weaker peaks in the turbulent velocity spectrum. Sharp-edged nozzles are thus suitable for applications requiring high centreline velocity and turbulent mixing under a fixed mass flow rate. In contrast, planar and filleted nozzles are preferable where lower flow-induced disturbances and controlled momentum flux are required.

### C. Aerodynamic noise

The aeroacoustic characteristics of the four cases are analysed to evaluate the influence of nozzle profile on noise generation. To visualize the acoustic propagation in the flow field, the contour of the divergence of the time-derivative of the velocity field ($\nabla \cdot \dot{U}$) for the four cases is presented in Fig. 17. The field contains both hydrodynamic and acoustic perturbations, which propagate at different speeds to the far field. The acoustic waves are identified through animations of $\nabla \cdot \dot{U}$ field. In all cases, wave fronts can be observed in the region $X/h < 15$, as indicated by

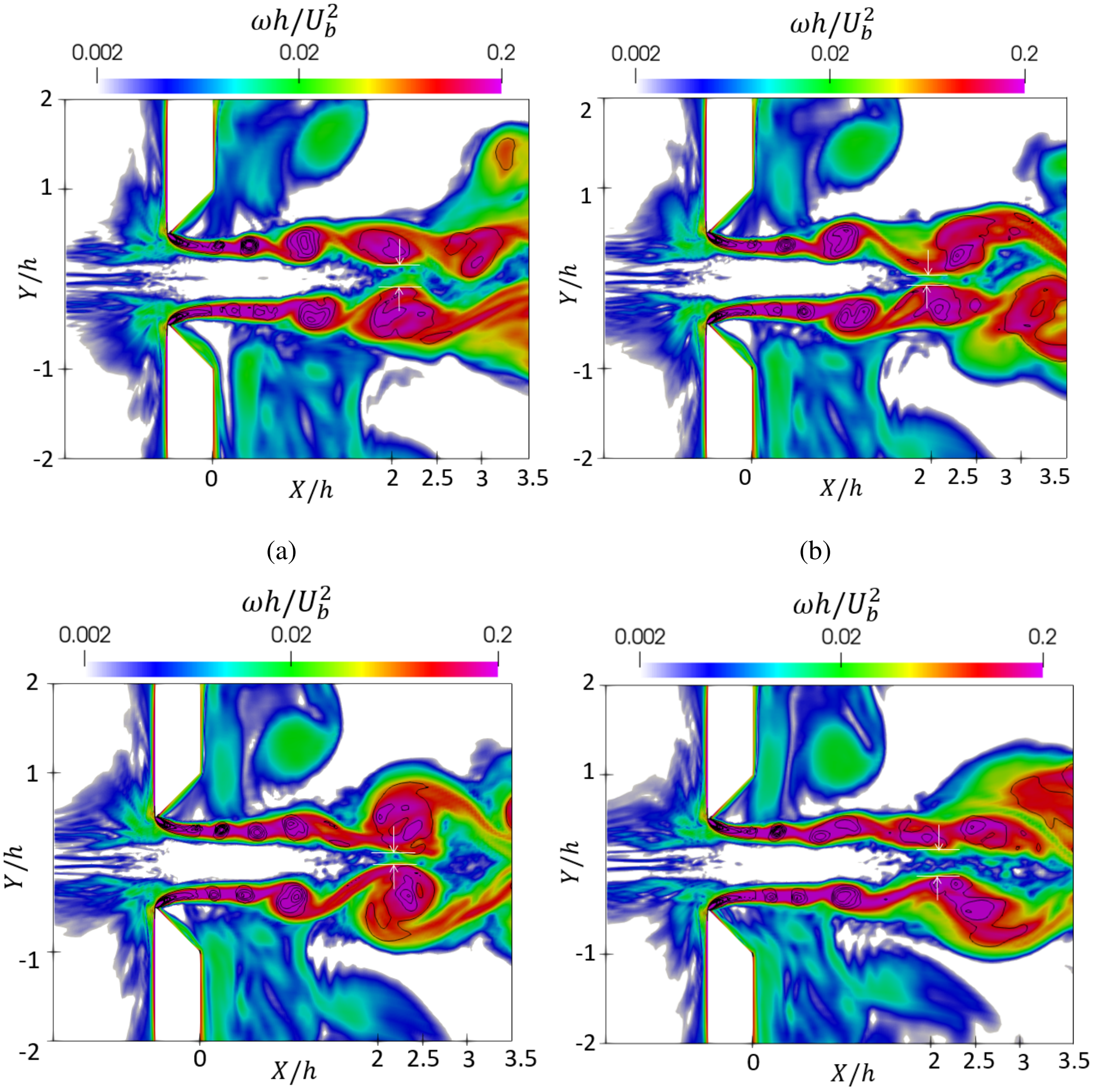

(a)

(b)

(c)

(d)

FIG. 16: The normalized vorticity field of bevelled nozzle at different timesteps. (a) $\Delta t^* = 0$; (b) $\Delta t^* = 2.4$; (c) $\Delta t^* = 4.8$; (d) $\Delta t^* = 7.2$.

the white arrows, propagating away from the jet towards the far field. The centre of these wave fronts are located near the jet centreline, specifically in the region of $X/h < 10$. Although this does not pinpoint the exact location of the sound generation, it strongly suggests that the noise source lies near the end of the potential core, where vortex interaction occurs, as shown in Fig. 12. This agrees with the findings of Laufer and Yen[50], who argued that, in circular jets at low Mach numbers, noise sources are concentrated near the end of the potential core.

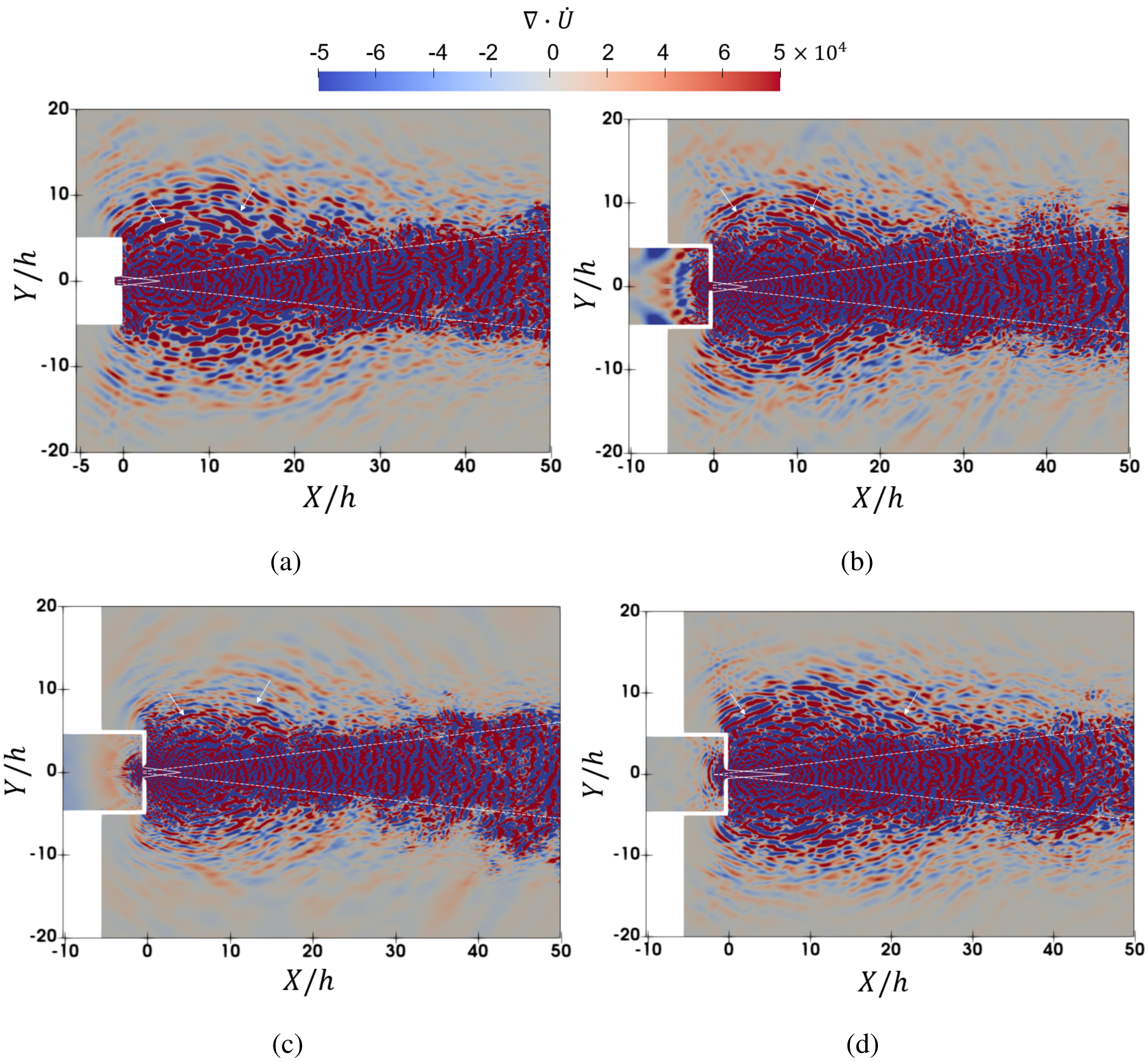

(a)

(b)

(c)

(d)

FIG. 17: Visualization of sound wave by divergence of the time-derivative of the velocity field ($\nabla \cdot \dot{\mathbf{U}}$) contour of (a) planar nozzle, (b) square orifice, (c) bevelled orifice, and (d) filleted orifice. The white solid lines are the inner mixing boundary and the dash lines denote the jet half-width.

The results of the FW-H permeable integration surface placement study, shown in Fig. 24 in Appendix B, are applied to all the acoustic calculations in this section. Nineteen receivers are uniformly positioned around the jet nozzle at angular positions ranging from $0^\circ < \theta < 180^\circ$ with a radial distance of 5 meters from the nozzle exit. Fig. 18 presents the narrowband noise spectra for the four different geometries at $\theta = 30^\circ$ and $90^\circ$. Notably, the noise spectra of the planar nozzle and the filleted orifice are broadband in nature. However, distinct peaks in the acoustic spectra are observed in the square and bevelled cases at frequencies of approximately 4.24 kHz, 8.44 kHz and 12.7 kHz at both angles. These peaks, previously seen in the turbulent velocity spectrum (shown in Fig. 14), are associated with vortex roll-up and interaction in the shear layer and importantly propagate into the far field as sound. However, although vortex roll-up and interactions etc. has been qualitatively identified in all four cases, these tonal peaks are unique to cases with sharp edges and a strong vena contraction, i.e. the square and bevelled orifices. This suggests that higher turbulence intensity, reduced shear layer spacing and synchronized vortex roll-up and shedding from both lips may be responsible for triggering these tonal noise components. Nevertheless, the threshold level of these influencing factors required to generate tonal peaks needs to be investigated in future work.

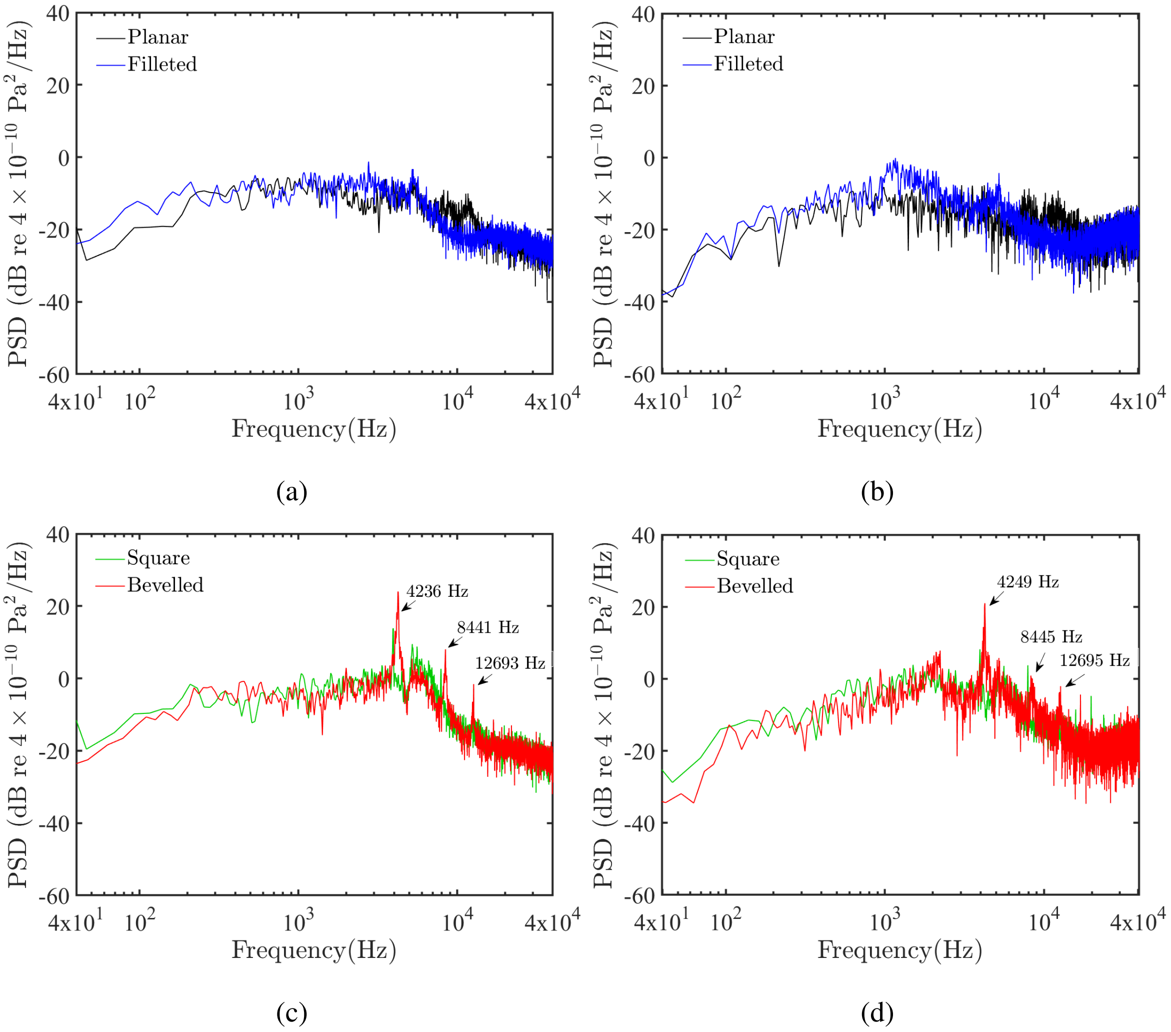

(a)

(b)

(c)

(d)

FIG. 18: Narrow-band noise spectra. (a) Planar nozzle and filleted orifice at 30°; (b) Planar nozzle and filleted orifice at 90°; (c) Square and bevelled orifices at 30°; (d) Square and bevelled orifices at 90°.

Fig. 19 presents noise directivity patterns for the four cases. The overall sound pressure level

(OASPL) is obtained by integrating the noise over the frequency range from 20 Hz to 20 kHz. In Fig. 19(a), the integration includes the entire frequency spectrum, incorporating both broadband and tonal components, as shown in Fig. 18. In contrast, Fig. 19(b), presents the OASPL with the tonal components excluded from the integration. This is to show the effect of nozzle type on the broadband noise. In Fig. 19(a), the OASPL for the bevelled and square orifices are approximate 10 dB higher than those of planar nozzle and the filleted orifice in all directions. The bevelled orifice is the loudest (in terms of OASPL) due to the loud tone previously discussed. The planar nozzle and filleted orifice have similar OASPL levels from 0° to 60°. This is expected as both the planar nozzle and filleted orifice exhibit similar mean velocity profiles, turbulence intensities (in both the streamwise and transverse directions), centreline decay rates, and near-field spreading rates.

In Fig. 19(b), the OASPLs (excluding the tonal contributions) show that the broadband noise of the square orifice is the loudest configuration. This is different to the conclusion of the OASPL over the entire frequency range due to the large tone seen in the bevelled orifice case. The broadband OASPL difference between the square orifice and the planar nozzle is approximately 7 dB, which is less than the OASPL when the tones are included in the integration (Fig. 19(a)). This is due to the pronounced tonal noise peaks induced by the sharp edge orifices, as shown previously in Fig. 18. It was shown previously that the sharp-edge cases (square and bevelled orifices) result in stronger turbulence intensity compared to the planar nozzle and the filleted orifice. These instabilities in the shear layer not only generate tonal peaks in the noise spectra but also increases the broadband noise.

To assess the sound power level (SWL) emitted from the four nozzle types, receivers are placed on a sphere with a radius of 5 m surrounding the jet. The sphere is divided into 384 segments and the receivers are located at the centre of the segments. The overall SWL (OASWL) is calculated by the following equations:

$$\mathrm{SWL}_i = 10\log_{10}\left(\sum_{j=1}^{384}\frac{p_{i,j}^2 A_j}{\rho c W_0}\right), \tag{9}$$

$$\mathrm{OASWL} = 10\log_{10}\left(\sum_{i=1}^{30}10^{\mathrm{SWL}_i/10}\right), \tag{10}$$

where $\mathrm{SWL}_i$ is the sound power level in the $i^{\mathrm{th}}$ one-third octave band, $p_{i,j}$ is the sound pressure on the $j^{\mathrm{th}}$ segment of the sphere in the $i^{\mathrm{th}}$ one-third octave band, $A_j$ is the area of $j^{\mathrm{th}}$ segment, $\rho$ is air density (1.225 kg/m$^3$), $c$ is the sound speed (345 m/s), and $W_0$ is the reference sound power ($1\times10^{-12}$ W). Fig. 20(a) presents the SWL spectra of the four cases, calculated using Eq. (9), over

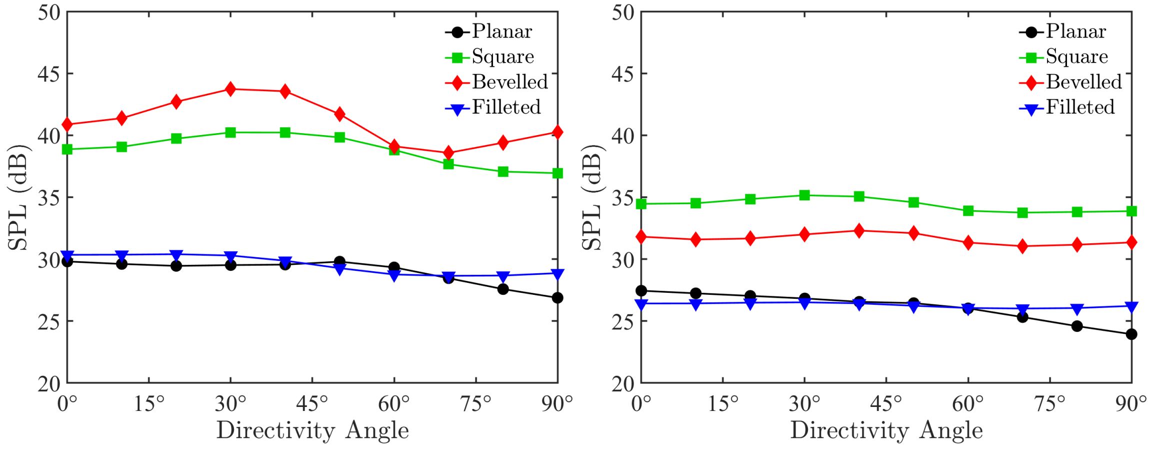

(a)

(b)

FIG. 19: Noise directivities of the planar nozzle, square, bevelled, and filleted orifices. (a) overall sound pressure level; (b) broadband overall sound pressure level with tones removed.

the frequency range from 40 Hz to 20 kHz. It can be observed that all four cases exhibit similar SWLs at frequencies below 500 Hz. However, the sharp-edge cases (bevelled and square orifices) show higher SWLs than the other two configurations across most of the higher frequency range, up to 20 kHz. This phenomenon is attributed to the vena contraction effect, which accelerates the jet exit velocity up to $1.5U_b$ and increases turbulence intensity, as shown in Fig. 10 and Fig. 11, which enhances the strength of the noise sources. This also results in higher overall sound power levels (OASWLs) for the sharp-edge cases compared to the planar nozzle and filleted orifice, as shown in Fig. 20(b).

The ranking of the nozzle cases in terms of overall sound power level in Fig. 20(b) is similar to that previously detailed in the broadband OASPL with the tonal components removed (Fig. 19(b)). While both sharp-edged cases have similar OASWL, the square orifice is 0.8 dB louder than the bevelled orifice. This ranking is different compared to the overall sound pressure level in Fig. 19(a), where the bevelled orifice was loudest. This difference is due to differences in the directivity of the tonal components of the sharp-edged cases. These tonal peaks are directional and when the overall sound power is calculated over all the directivities, their relative contribution to the overall sound power level becomes less. As a result, when considering only the broadband components, the planar nozzle exhibits the lowest OASWLs (approximately 1.5 dB lower than that of the filleted nozzle). While similar, this difference can be attributed to the slight vena contraction that also occurs in the filleted nozzle, although it is much weaker than that observed in the sharp-edged cases.

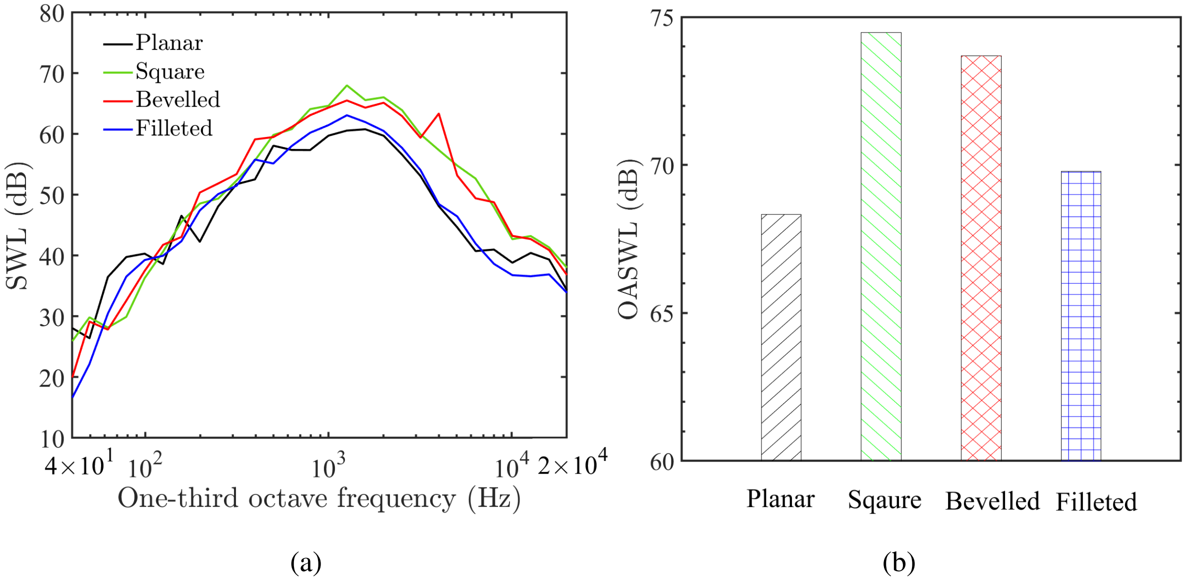

FIG. 20: Sound power levels of the four types of nozzle. (a) sound power spectra in one-third octave; (b) overall sound power level.

## V. CONCLUSION

This numerical study examined the influence of nozzle geometry on the near-field turbulence, jet dynamics, and aerodynamic noise of rectangular jets. Four configurations were analyzed. These were a planar nozzle, a square-edge orifice, a bevelled-edge orifice, and a filleted-edge orifice. The mass flow rate was the same for each of the four nozzles allowing the effect of nozzle geometry to be isolated. The conditions were a Reynolds number of $Re = 10^4$ and a Mach number of $Ma \approx 0.17$. The DDES coupled with the FW-H acoustics solver showed good agreement with experimental data, validating the numerical framework for low-Mach number rectangular jets.

Results demonstrated that nozzle geometry significantly affects both flow development and acoustic emission. Sharp-edged nozzles (square and bevelled) produce strong vena contractions, increasing the exit velocity (up to $1.5U_b$) and turbulence intensity, resulting in shorter potential cores compared to the filleted case. The filleted nozzle weakens this contraction, extending the potential core ($7.5h$ versus $4h$, for sharp-edge cases) and reducing turbulence. The planar nozzle exhibits a fully developed inlet profile and lower turbulence intensity than the sharp-edged cases. Sharp-edged nozzles generate stronger vorticity and higher spreading rates ($K_{1u} = 0.118$ versus

0.100 for the planar case). Enhanced vortex roll-up and shear-layer interaction in these cases increase turbulent mixing, rapidly broadening the jet half-width beyond $X/h > 4$.

Analysis of the turbulent velocity spectrum revealed a tonal peak at 4.3 kHz and its harmonics (8.5 kHz and 12.7 kHz) for the bevelled-edge nozzle. This tone was linked to vortex interactions between the two shear layers in the jet. For the bevelled case, the vortices from both shear layers roll-up and propagate in phase between the upper and lower shear layers. Such in-phase vortex motion was only observed in the bevelled case. The strong vena contraction in the bevelled case resulted in stronger shear layers and reduced the distance between the two shear layers increasing this interaction effect. The square orifice showed weaker peaks, while the planar and filleted nozzles exhibited broadband turbulent velocity spectra due to lower turbulence intensity and less coherent vortex roll-up. SPOD for the bevelled case identified these tonal frequencies as coherent modes contained within the region $h < X < 4h$.

These tones in the turbulent velocity spectra propagate to the far field as acoustic waves. The bevelled nozzle produces distinct tonal peaks at the same frequencies as in the turbulent velocity spectra. The square nozzle exhibits much milder tones, and the planar and filleted nozzles generate broadband noise. Sharp-edged nozzles (bevelled and square) yield OASPLs approximately 10 dB higher than the others (planar and filleted), primarily due to the vena contraction effects that increase exit velocity by up to $1.5U_b$. The bevelled nozzle is the loudest due to its strong tone due to the shear layer interactions in the jet. When considering only the broadband noise, the sharp-edged nozzles remain approximately 7 dB louder compared to the filleted and planar cases. A similar trend is observed in OASWLs. Specifically, the OASWL of the square nozzle is about 0.8 dB higher than that of the bevelled nozzle, while the filleted nozzle has an OASWL approximately 1.5 dB higher than the planar case.

Overall, the findings demonstrate that nozzle geometry strongly influences both aerodynamic performance and noise generation at a constant mass flow rate. Sharp-edged nozzles enhance shear-layer mixing but produce higher noise levels, whereas planar and filleted designs offer quieter operation with reduced turbulent mixing. These results underscore the importance of nozzle geometry in balancing aerodynamic efficiency and acoustic performance. They also provide valuable guidance for optimizing nozzle profiles in applications such as aviation, high-speed transport, and HVAC systems, where minimizing noise while maintaining sufficient turbulent mixing, length of the potential core and jet centreline velocity is essential.

## DECLARATION OF COMPETING INTEREST

The authors declare that there is no known competing financial interests or personal relationships that could have appeared to influence the work reported in this manuscript.

## ACKNOWLEDGEMENTS

All simulations were conducted on Iridis5 supercomputer at the University of Southampton.

## APPENDIX A: ADDITIONAL DETAILS FOR THE PRECURSOR SIMULATION

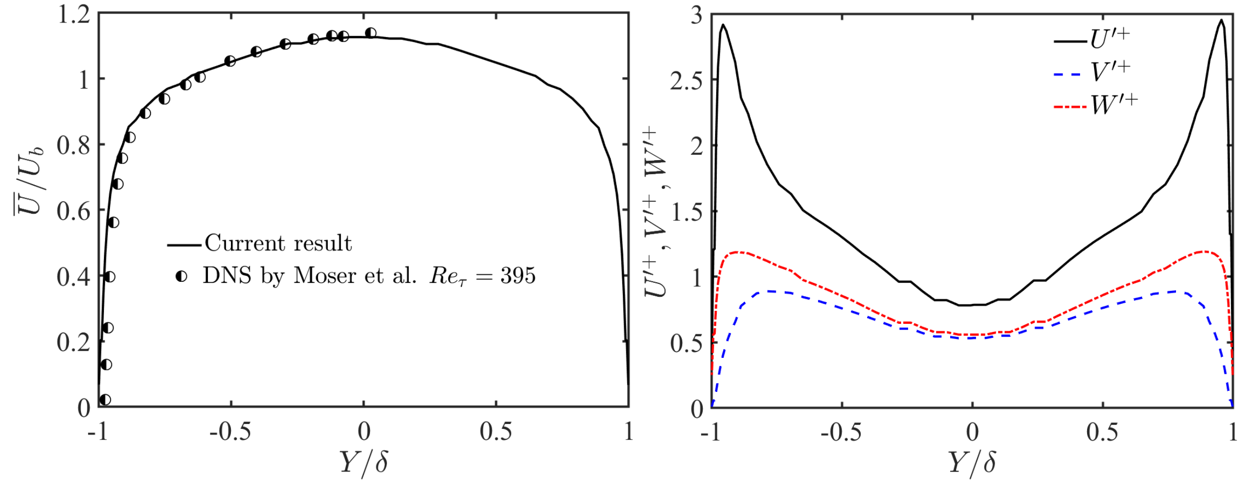

(a)

(b)

FIG. 21: Velocity profiles of the inlet velocity field for the channel flow case. (a) Dimensionless time-averaged velocity profile at the centre of the channel. The experimental data is from Moser et al.[51]; (b) Turbulence intensity profiles normalized by $u_\tau = \sqrt{\tau_w/\rho}$, where $\tau_w$ is wall shear stress and $\rho$ is the density.

The height of the channel is identical to the jet height (4 mm) and its length in the streamwise direction is 10 mm. To ensure the development of a fully turbulent and statistically steady channel flow, periodic boundary conditions were applied between the inlet and outlet of the channel. The resulting velocity profile is presented in Fig. 21, where the mean dimensionless streamwise velocity ($\overline{U}/U_b$) profile in Fig. 21(a) demonstrates excellent agreement with the DNS data for channel flow at $\mathrm{Re}_\tau = 395$. Fig. 21(b) depicts the turbulence intensity of the developed channel flow. The turbulence intensity profiles ($U', V', W'$) are normalized by $u_\tau = \sqrt{\tau_w/\rho}$, where $\tau_w$ is wall shear stress and $\rho$ is the air density.

## APPENDIX B: ADDITIONAL DETAILS ON GRID RESOLUTION AND VALIDATION

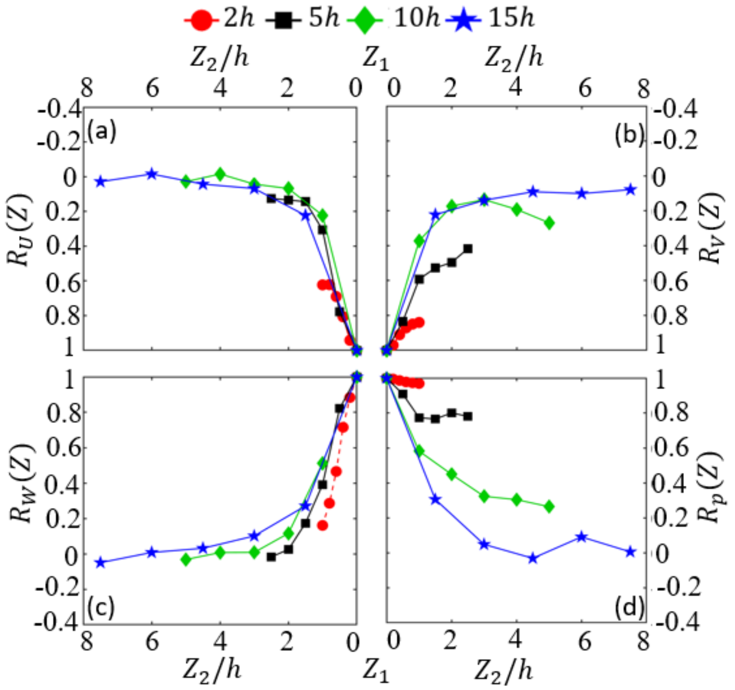

FIG. 22: Correlation coefficients of velocity and pressure with different spanwise lengths. (a) Correlation coefficient of streamwise velocity, $U$; (b) correlation coefficient of transverse velocity, $V$ (c) correlation coefficient of spanwise velocity, $W$; (d) correlation coefficient of pressure, $p$.

To ensure that the spanwise variations are adequately captured within the chosen spanwise extent, the correlation between the mid-plane and the periodic plane should naturally decay to zero. To evaluate this, the correlation coefficient is calculated as follows,

$$R_\phi(Z) = \frac{\mathrm{cov}(\phi_{Z_1}, \phi_{Z_2})}{\sigma(\phi_{Z_1}) \cdot \sigma(\phi_{Z_2})}, \tag{11}$$

where $R_\phi(Z)$ is the correlation coefficient in the $Z$-direction, $\phi$ is the flow field variable, $\mathrm{cov}(\phi_{Z_1}, \phi_{Z_2})$ is the covariance of $\phi$ at $Z_1$ and $Z_2$, and $\sigma(\phi)$ represents the standard deviation of $\phi$ at these positions. The subscripts $Z_1$ and $Z_2$ denote different positions in the $Z$-direction.

To justify an adequate spanwise length of the simulations, the spanwise correlation coefficients were calculated for four cases with spanwise lengths of $2h$, $5h$, $10h$, and $15h$. Six monitors were positioned 35$h$ downstream from the jet exit on the centreline, uniformly distributed from the mid-plane to the periodic plane for each case. The correlation coefficients $R_\phi(Z)$ for velocity and pressure are shown in Fig. 22. The monitor on the mid-plane is denoted as $Z_1$, while $Z_2$ represents the positions of the remaining monitors along the spanwise direction. As shown in Fig. 22, $R_\phi(Z)$ decays as $Z_2$ approaches the periodic plane for all cases. However, for the cases with spanwise lengths of 2$h$ and 5$h$, the values of $R_\phi(Z)$ remain significantly above zero when $Z_2$ is located on the periodic plane.

Fig. 23 shows the arrangement of the FW-H permeable integration surfaces placement study. The permeable surfaces fully enclose the turbulent wake of the jet until $x/h = 35$, ensuring the primary noise-generating regions are captured. The positions of the integral surface are carefully placed within the refined computational region. This refinement region can resolve frequencies up to approximately 20 kHz assuming 20 points per wavelength. The receiver is placed on the mid-plane at the position ($r = 5$ m and $\theta = 60°$) (see Fig. 3).

Fig. 24 compares the noise spectra of three different permeable FW-H surfaces of the case with a spanwise length of 10$h$. The results presented here correspond to a receiver at $\theta = 30°$, $\theta = 60°$ and $\theta = 90°$. The results show that the noise spectra of case Surf 2 and Surf 3 are similar, whereas Surf 1 exhibits significant deviations in both the low and high-frequency ranges. This discrepancy can be attributed to the fact that Surf 2 and Surf 3 encompass more acoustic noise sources.

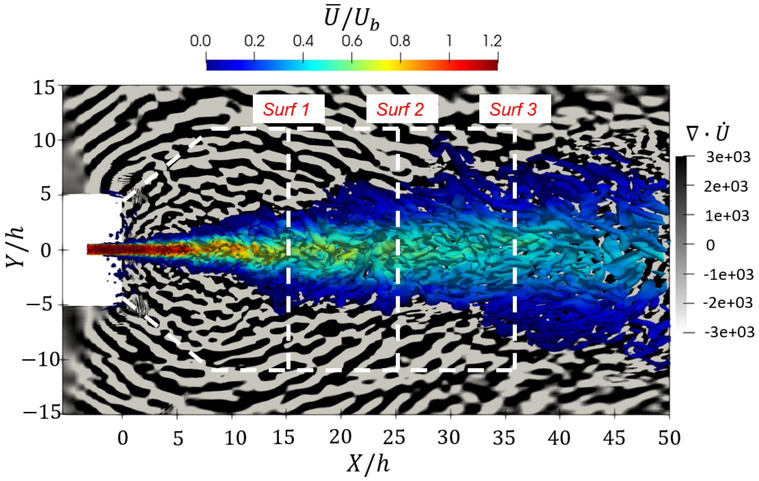

FIG. 23: The FW-H integral surface for the case with spanwise length of 10$h$ shown alongside the normalized $Q$ criterion (0.01) and divergence of velocity derivative $\nabla \cdot \dot{\mathbf{U}}$.

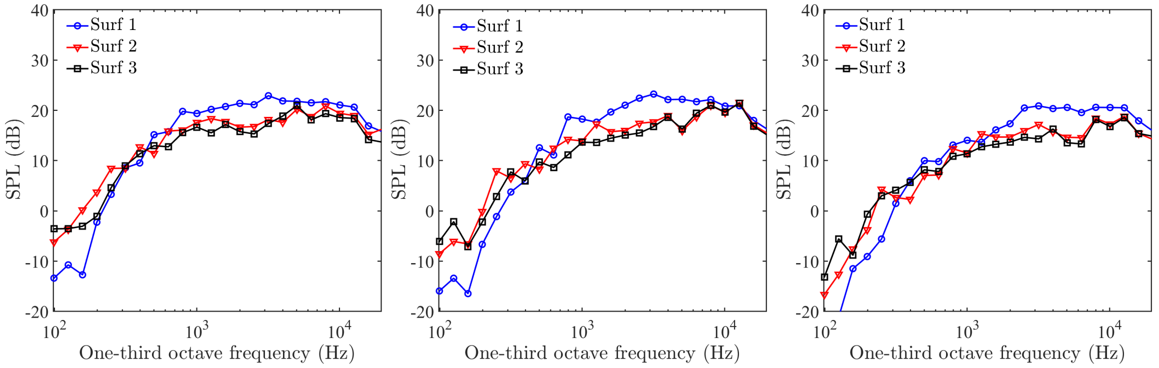

(a) (b) (c)

FIG. 24: Comparison of far field noise spectra at (a)$\theta = 30^\circ$, (b)$\theta = 60^\circ$ and (c)$\theta = 90^\circ$ with different FW-H integral surfaces.

## REFERENCES

[1] K. Kanjere, D. Angland, and X. Zhang. A numerical study to optimise blowing flow control for flap side-edge noise reduction. In *18th AIAA/CEAS Aeroacoustics Conference*, pages AIAA 2012–2097, 2012.

[2] K. Zhao, S. Alimohammadi, P. N. Okolo, J. Kennedy, and G. J. Bennett. Aerodynamic noise reduction using dual-jet planar air curtains. *Journal of Sound and Vibration*, 432:192–212, 2018. doi:10.1016/j.jsv.2018.06.036.

[3] Y. He. *Aerodynamic noise simulation of high-speed train bogie*. PhD thesis, University of Southampton, 2023.

[4] N. L. Keegan. Children who say hand dryers 'hurt my ears' are correct: A real-world study examining the loudness of automated hand dryers in public places. *Paediatrics & Child Health*, 25(4):216–221, 2020.

[5] S. Liu, X. Zhang, Y. Yuan, J. Lv, and L. Hu. Combustion characteristics and entrainment behavior of rectangular jet flame in cross airflow. *Energy*, 320:135375, 2025.

[6] P. Zhang, Z. Li, and S. A. Abdollahi. Computational modeling of the rectangular non-aligned multi-injector for efficient fuel mixing in a supersonic combustion chamber. *Scientific Reports*, 14(1):15959, 2024. doi:10.1038/s41598-024-66309-1.

[7] Y. Wu, Guangnian Ji, Peizhi Zhang, Xiaoquan Yang, and Jue Ding. Numerical study of flow and noise control mechanism of shape-optimized series cylinder. *Journal of Aerospace Engineering*, 37(6):04024080, 2024. doi:10.1061/JAEEEZ.ASENG-5625.

[8]C. Y. Zhang, Xiao-hui Xiong, Guang Chen, and Bo Chen. Numerical study on passive flow and noise control of finite wall-mounted cylinder with porous coatings. *Physics of Fluids*, 37, 2025.

[9]A. Scala, G. Paolillo, C. S. Greco, T. Astarita, and G. Cardone. Genetically-based active flow control of a circular cylinder wake via synthetic jets. *Experimental Thermal and Fluid Science*, 162:111362, 2025. doi:10.1016/j.expthermflusci.2024.111362.

[10]Xiaojun Chen, Yueping Guo, Hui Zhang, and Yujie Zhou. Passive jet control of flow around a circular cylinder. *Experiments in Fluids*, 56(10):207, 2015. doi:10.1007/s00348-015-2077-5.

[11]A. Sfeir. The velocity and temperature fields of rectangular jets. *International Journal of Heat and Mass Transfer*, 19(11):1289–1297, 1976.

[12]A. Sfeir. Investigation of three-dimensional turbulent rectangular jets. *AIAA Journal*, 17(10): 1055–1060, 1979.

[13]W. Quinn. Turbulent free jet flows issuing from sharp-edged rectangular slots: the influence of slot aspect ratio. *Experimental Thermal and Fluid Science*, 5(2):203–215, 1992.

[14]R. C. Deo, J. Mi, and G. J. Nathan. The influence of nozzle aspect ratio on plane jets. *Experimental Thermal and Fluid Science*, 31(8):825–838, 2007.

[15]W. Quinn. Development of a large-aspect-ratio rectangular turbulent free jet. *AIAA Journal*, 32 (3):547–554, 1994.

[16]R. C. Deo, J. Mi, and G. J. Nathan. The influence of reynolds number on a plane jet. *Physics of Fluids*, 20(7), 2008.

[17]J. Mi, M. Xu, and T. Zhou. Reynolds number influence on statistical behaviors of turbulence in a circular free jet. *Physics of Fluids*, 25(7), 2013.

[18]R. C. Deo, J. Mi, and G. J. Nathan. The influence of nozzle-exit geometric profile on statistical properties of a turbulent plane jet. *Experimental Thermal and Fluid Science*, 32(2):545–559, 2007.

[19]A. Abdel-Rahman. A review of effects of initial and boundary conditions on turbulent jets. *WSEAS Transactions on Fluid Mechanics*, 4(5):257–275, 2010.

[20]C. Le Ribault, S. Sarkar, and S. Stanley. Large eddy simulation of a plane jet. *Physics of Fluids*, 11(10):3069–3083, 1999.

[21]C. Le Ribault, S. Sarkar, and S. Stanley. Large eddy simulation of evolution of a passive scalar in plane jet. *AIAA Journal*, 39(8):1509–1516, 2001.

[22]S. Matsuyama. Implicit large-eddy simulation of turbulent plane jet at re = $10^4$. *Computers & Fluids*, 250:105732, 2023. doi:10.1016/j.compfluid.2022.105732.

[23]B. Rembold, N. A. Adams, and L. Kleiser. Direct numerical simulation of a transitional rectangular jet. *International Journal of Heat and Fluid Flow*, 23(5):547–553, 2002. doi: 10.1016/S0142-727X(02)00150-9.

[24]E. Faghani, R. Maddahian, P. Faghani, and B. Farhanieh. Numerical investigation of turbulent free jet flows issuing from rectangular nozzles: the influence of small aspect ratio. *Archive of Applied Mechanics*, 80(7):727–745, 2010.

[25]P. Jiang, Y. C. Guo, C. K. Chan, and W. Y. Lin. Frequency characteristics of coherent structures and their excitations in small aspect-ratio rectangular jets using large eddy simulation. *Computers & Fluids*, 36(3):611–621, 2007. doi:10.1016/j.compfluid.2006.05.001.

[26]Peter Jordan and Tim Colonius. Wave packets and turbulent jet noise. *Annual Review of Fluid Mechanics*, 45:173–195, 2013. doi:10.1146/annurev-fluid-011212-140756.

[27]Oliver T Schmidt, Aaron Towne, Georgios Rigas, Tim Colonius, and Beverley J McKeon. Wavepackets and trapped acoustic modes in a turbulent jet: Coherent structure eduction and global stability. *Journal of Fluid Mechanics*, 825:1153–1181, 2018. doi:10.1017/jfm.2017.502.

[28]Guillaume A Brès, Peter Jordan, Maxime Le Rallic, Vincent Jaunet, and Tim Colonius. Importance of the nozzle-exit boundary-layer state in subsonic turbulent jet noise. *Journal of Fluid Mechanics*, 851:83–124, 2018. doi:10.1017/jfm.2018.513.

[29]L. J. S. Bradbury. The structure of a self-preserving turbulent plane jet. *Journal of Fluid Mechanics*, 23(1):31–64, 1965. doi:10.1017/S0022112065001222.

[30]P. R. Spalart. Comments on the feasibility of les for wings, and on a hybrid rans/les approach. *Advances in DNS/LES*, pages 137–147, 1997.

[31]F. Menter and M. Kuntz. Adaptation of eddy-viscosity turbulence models to unsteady separated flow behind vehicles. In *The aerodynamics of heavy vehicles: trucks, buses, and trains*, pages 339–352. Springer, 2004.

[32]F. R. Menter, M. Kuntz, and R. Langtry. Ten years of industrial experience with the sst turbulence model. In *Turbulence, Heat and Mass Transfer*, volume 4, pages 625–632, 2003.

[33]P. R. Spalart, S. Deck, M. L. Shur, K. D. Squires, M. K. Strelets, and A. Travin. A new version of detached-eddy simulation, resistant to ambiguous grid densities. *Theoretical and Computational Fluid Dynamics*, 20(3):181, 2006. doi:10.1007/s00162-006-0015-0.

[34]Y. He, D. Thompson, and Z. Hu. Aerodynamic noise from a high-speed train bogie with complex geometry under a leading car. *Journal of Wind Engineering and Industrial Aerodynamics*, 244: 105617, 2024.

[35] X. Liu, D. J. Thompson, and Z. Hu. Numerical investigation of aerodynamic noise generated by circular cylinders in cross-flow at reynolds numbers in the upper subcritical and critical regimes. *International Journal of Aeroacoustics*, 18(4-5):470–495, 2019.

[36] Y. Wang, B. Ma, Z. Hu, and D. Thompson. Characteristics of the flow around finite wall-mounted square cylinders and the mechanism of tonal noise. *Physics of Fluids*, 36(6), 2024.

[37] F. Farassat. Derivation of formulations 1 and 1a of farassat. Technical report, NASA, 2007.

[38] T. J. Poinsot and S. K. Lelef. Boundary conditions for direct simulations of compressible viscous flows. *Journal of Computational Physics*, 101(1):104–129, 1992. doi:10.1016/0021-9991(92)90046-2.

[39] P. R. Spalart. Strategies for turbulence modelling and simulations. *International Journal of Heat and Fluid Flow*, 21(3):252–263, 2000.

[40] N. J. Georgiadis, D. P. Rizzetta, and C. Fureby. Large-eddy simulation: current capabilities, recommended practices, and future research. *AIAA Journal*, 48(8):1772–1784, 2010.

[41] S. Munro and K. Ahuja. Aeroacoustics of a high aspect-ratio jet. In *9th AIAA/CEAS Aeroacoustics Conference and Exhibit*, 2003.

[42] A. Krothapalli, D. Baganoff, and K. Karamcheti. On the mixing of a rectangular jet. *Journal of Fluid Mechanics*, 107:201–220, 1981.

[43] O. T. Schmidt, A. Towne, G. Rigas, T. Colonius, and G. A. Brès. Spectral analysis of jet turbulence. *Journal of Fluid Mechanics*, 855:953–982, 2018. doi:10.1017/jfm.2018.675.

[44] A. Ghasemi. *Near-field Vortex Dynamics of Flows Emerging from a Rectangular Duct*. PhD thesis, University of Adelaide, 2019.

[45] A. Nekkanti, T. Colonius, and O. T. Schmidt. Nonlinear dynamics of vortex pairing in transitional jets. *arXiv preprint arXiv:2407.16851*, 2024.

[46] J. L. Lumley. *Stochastic tools in turbulence*. Academic Press, 1970.

[47] O. T. Schmidt and T. Colonius. Guide to spectral proper orthogonal decomposition. *AIAA Journal*, 58(3):1023–1033, 2020.

[48] M. Sieber, C. O. Paschereit, and K. Oberleithner. Spectral proper orthogonal decomposition. *Journal of Fluid Mechanics*, 792:798–828, 2016. doi:10.1017/jfm.2016.103.

[49] A. Towne, O. T. Schmidt, and T. Colonius. Spectral proper orthogonal decomposition and its relationship to dynamic mode decomposition and resolvent analysis. *Journal of Fluid Mechanics*, 847:821–867, 2018. doi:10.1017/jfm.2018.283.

[50] J. Laufer and T.-C. Yen. Noise generation by a low-mach-number jet. *Journal of Fluid Mechan-*

*ics*, 134:1–31, 1983.

[51] R. D. Moser, J. Kim, and N. N. Mansour. Direct numerical simulation of turbulent channel flow up to re = 590. *Physics of Fluids*, 11(4):943–945, 1999.